The Astrophysical Journal, 707:1201–1216, 2009 December 20 doi:10.1088/0004-637X/707/2/1201

THE LARGE APEX BOLOMETER CAMERA SURVEY OF THE EXTENDED CHANDRA DEEP FIELD SOUTH

A. Weiß[1], A. Kovács[1], K. Coppin[2], T. R. Greve[3], F. Walter[3], Ian Smail[2], J. S. Dunlop[4], K. K. Knudsen[5], D. M. Alexander[6], F. Bertoldi[5], W. N. Brandt[7], S. C. Chapman[8], P. Cox[9], H. Dannerbauer[3], C. De Breuck[10], E. Gawiser[11], R. J. Ivison[4,12], D. Lutz[13], K. M. Menten[1], A. M. Koekemoer[14], E. Kreysa[1], P. Kurczynski[11], H.-W. Rix[3], E. Schinnerer[3], and P. P. van der Werf[15]

[1] Max-Planck Institut für Radioastronomy, Auf dem Hügel 69, 53121 Bonn, Germany
[2] Institute for Computational Cosmology, Durham University, South Road, Durham, DH1 3LE, UK
[3] MPIA, Königstuhl 17, 69117 Heidelberg, Germany
[4] Institute for Astronomy, University of Edinburgh, Royal Observatory, Blackford Hill, Edinburgh, EH9 3HJ, UK
[5] Argelander Institute for Astronomy, University of Bonn, Auf dem Hügel 71, D-53121 Bonn, Germany
[6] Department of Physics, Durham University, South Road, Durham, DH1 3LE, UK
[7] Department of Astronomy and Astrophysics, 525 Davey Lab, Pennsylvania State University, University Park, PA 16802, USA
[8] Institute of Astronomy, Madingley Road, Cambridge, CB3 0HA, UK
[9] Institut de Radio Astronomie Millimetrique, 300 Rue de la Piscine, Domaine Universitaire, 38406 Saint Martin d'Héres, France
[10] European Southern Observatory, Karl-Schwarzschild Strasse, 85748 Garching bei München, Germany
[11] Yale Center for Astronomy and Astrophysics, Yale University, New Haven, CT 06520, USA
[12] UK Astronomy Technology Centre, Royal Observatory, Blackford Hill, Edinburgh, EH9 3HJ, UK
[13] Max-Planck-Institut für extraterrestrische Physik, Postfach 1312, 85741 Garching, Germany
[14] Space Telescope Science Institute, 3700 San Martin Drive, Baltimore, MD 21218, USA
[15] Leiden Observatory, Leiden University, P.O. Box 9513, NL-2300 RA Leiden, The Netherlands
Received 2009 July 31; accepted 2009 October 28; published 2009 December 3

ABSTRACT

We present a sensitive 870 μm survey of the Extended Chandra Deep Field South (ECDFS) combining 310 hr of observing time with the Large Apex BOlometer Camera (LABOCA) on the APEX telescope. The LABOCA ECDFS Submillimetre Survey (LESS) covers the full $30' \times 30'$ field size of the ECDFS and has a uniform noise level of $\sigma_{870\,\mu\mathrm{m}} \approx 1.2$ mJy beam^{-1}. LESS is thus the largest contiguous deep submillimeter survey undertaken to date. The noise properties of our map show clear evidence that we are beginning to be affected by confusion noise. We present a catalog of 126 submillimeter galaxies (SMGs) detected with a significance level above 3.7σ, at which level we expect five false detections given our map area of 1260 arcmin^2. The ECDFS exhibits a deficit of bright SMGs relative to previously studied blank fields but not of normal star-forming galaxies that dominate the extragalactic background light (EBL). This is in line with the underdensities observed for optically defined high redshift source populations in the ECDFS (BzKs, DRGs, optically bright active galactic nucleus, and massive K-band-selected galaxies). The differential source counts in the full field are well described by a power law with a slope of $\alpha = -3.2$, comparable to the results from other fields. We show that the shape of the source counts is not uniform across the field. Instead, it steepens in regions with low SMG density. Towards the highest overdensities we measure a source-count shape consistent with previous surveys. The integrated 870 μm flux densities of our source-count models down to $S_{870\,\mu\mathrm{m}} = 0.5$ mJy account for >65% of the estimated EBL from *COBE* measurements. We have investigated the clustering of SMGs in the ECDFS by means of a two-point correlation function and find evidence for strong clustering on angular scales $<1'$ with a significance of 3.4σ. Assuming a power-law dependence for the correlation function and a typical redshift distribution for the SMGs we derive a characteristic angular clustering scale of $\theta_0 = 14'' \pm 7''$ and a spatial correlation length of $r_0 = 13 \pm 6\,h^{-1}$ Mpc.

Key words: cosmology: observations – galaxies: evolution – galaxies: high-redshift – galaxies: starburst – submillimeter – surveys

Online-only material: color figures, machine-readable table

1. INTRODUCTION

One of the most significant findings of the *IRAS* survey was the identification of a population of ultraluminous infrared galaxies (ULIRGs) that emit the bulk of their bolometric luminosity at far-IR wavelengths (Sanders & Mirabel 1996). Surveys in the submillimeter and millimeter wavebands over the past decade have shown that ULIRGs are much more common at high redshift compared to the local universe (e.g., Barger et al. 1999; Cowie et al. 2002; Borys et al. 2003; Webb et al. 2003; Greve et al. 2004; Laurent et al. 2005; Coppin et al. 2006; Pope et al. 2006; Bertoldi et al. 2007; Beelen et al. 2008; Knudsen et al. 2008; Scott et al. 2008; Austermann et al. 2009). These surveys show that the comoving volume density of luminous submillimeter galaxies (SMGs) increases by a factor of 1000 out to $z \sim 2$ (Chapman et al. 2005). Therefore luminous obscured galaxies at high redshift could dominate the total bolometric emission of galaxies at those epochs (Blain et al. 1999; Le Floch et al. 2005)

The identification and study of submillimeter galaxies has proved challenging since their first detection. The limited mapping speed of typical (sub)millimeter bolometer cameras meant that only few very bright examples have been found, although gravitational lensing initially aided somewhat (e.g., Smail et al. 1997; Ivison et al. 1998). Attempts to map large fields at submillimeter wavelengths have involved the use of patchworks of small "jiggle" maps (e.g., Coppin et al. 2006) or mixtures of single-bolometer photometry, small jiggle maps, and shallow scan maps used to construct a "Super-map" of GOODS-N (Borys et al. 2003; Pope et al. 2006). Both of

these approaches raise concerns about the homogeneity of the resulting maps and hence the reliability of the resulting source catalogs. Scan maps, where the array is continuously moved on the sky to trace out a closed pattern, should result in much more homogeneous coverage and mapping, while at the same time allowing for a reliable removal of the bright emission from the atmosphere. This technique has been used at submillimeter and millimeter wavelengths (e.g., at 350 μm, Kovács et al. 2006; at 1100 μm, Austermann et al. 2009), however, no deep survey have employed such a technique in the 870 μm window where most of the published work on SMGs has been undertaken. Drawing this distinction between 870 μm and 1100 μm surveys may appear surprising given the modest difference between the two wavelengths and the assumed unstructured nature of the dust spectrum at these wavelengths. Despite only a 25% difference in the two wavelengths, there are hints of significant differences in the populations identified at 870 μm and 1100 μm (e.g., Greve et al. 2004; Younger et al. 2008), although these may in turn reflect the different mapping techniques used in individual studies.

The advent of the new Large APEX Bolometer Camera (LABOCA; Siringo et al. 2009), with an instantaneous 11.′4 field of view, on the 12 m APEX telescope (Güsten et al. 2006) provided the opportunity to undertake the first sensitive and uniform panoramic survey of the extragalactic sky at 870 μm. To exploit this opportunity a number of groups within the Max Planck Gesellschaft (MPG) and the European Southern Observatory (ESO) communities proposed a joint public legacy survey of the Extended Chandra Deep Field South (hereafter ECDFS) to the MPG and ESO time allocation committees: the LABOCA ECDFS submillimetre survey (LESS). The ECDFS covers a $0.^{\circ}5 \times 0.^{\circ}5$ region centered on the Chandra Deep Field South (CDFS) at R.A. $03^{\rm h}32^{\rm m}28.^{\rm s}0$, decl. $-27^{\circ}48'30.''0$. This field has very low far-infrared backgrounds and good ALMA visibility and hence has become one of the pre-eminent fields for cosmological survey science. As a result, the ECDFS is unique in the southern hemisphere in the combination of area, depth, and spatial resolution of its multiwavelength coverage from X-rays through optical, near-, and mid-infrared to the far-infrared and radio regimes. The central part of this field is coincident with the CDFS (Giacconi et al. 2002) which has now reached a depth of 2 Ms (Luo et al. 2008) and the deep *Hubble Space Telescope* (*HST*) imaging of the GOODS-S field (Giavalisco et al. 2004) and the Hubble Ultra Deep Field (UDF; Beckwith et al. 2006). In addition to the extremely deep observations of the central regions of this field as part of the CDFS, GOODS, and Hubble UDF surveys, the full $0.^{\circ}5$ field has extensive multiwavelength imaging available including: 250 ks *Chandra* integrations over the whole field (Lehmer et al. 2005); deep and multi-band optical imaging by COMBO-17 (Wolf et al. 2004, 2008) and MUSYC (Gawiser et al. 2006) including *HST* imaging for the GEMS project (Caldwell et al. 2008); near-infrared imaging by MUSYC (Taylor et al. 2009); deep mid-infrared imaging with Infrared Array Camera (IRAC) as part of SIMPLE (Damen et al. 2009) and using the MIPS instrument at 24, 70, and 160 μm by FIDEL (M. Dickinson et al. 2009, in preparation). Longer wavelength coverage comes from BLAST (Devlin et al. 2009) at 250, 350, and 500 μm (and in the near future from *Herschel*), while radio coverage of this field is reported by Miller et al. (2008) and Ivison et al. (2009).

The LABOCA survey of the ECDFS adds a waveband that pin points the thermal emission from luminous dusty galaxies at $z \sim 1$–8: a powerful addition to this singularly well-studied region—ideally placed for VLT observations and early science follow-up with ALMA. The completed LESS project provides a representative, homogeneous, and statistically-reliable sample of the SMGs with the high-quality, multiwavelength data required to yield identifications, constrain their redshifts, bolometric luminosities and power sources and hence determine their contribution to the total star formation density at high redshift. These sources can be related in unprecedented precision to other populations of active galactic nuclei (AGNs) and galaxies within the same volume to understand the place of SMGs in the formation and evolution of massive galaxies at high redshift. The survey is also sufficiently large that it should also yield examples of rare classes of SMGs, such as very high redshift sources, $z > 4$ (Coppin et al. 2009). These same data also provide submillimeter coverage of large numbers of high-redshift galaxies and AGNs to determine their bulk submillimeter properties from the stacking analysis of sub-samples as a function of population, redshift, environment, etc. (Greve et al. 2009; D. Lutz et al. 2009, in preparation). Together, these two techniques allow us to sample two orders of magnitude in bolometric luminosity—from hyperluminous infrared galaxies with $10^{13}\,L_{\odot}$ which are directly detected in the LABOCA maps, down to luminous infrared galaxies at $10^{11}\,L_{\odot}$ which are detected statistically through stacking. This range in luminosity encompasses the variety of populations expected to dominate the bolometric emission at $z \sim 1$–3 and the cosmic submillimeter background.

In this paper, we present a detailed description of the observations, reduction, and analysis of the LABOCA observations of the ECDFS and the resulting catalog of submillimeter galaxies. The observations are described in Section 2, Section 3 presents our results and we discuss these in Section 4. Finally, in Section 5, we give our summary and the main conclusions of this work. We assume a cosmology with $H_0 = 70$ km s^{-1} Mpc^{-1}, $\Omega_{\Lambda} = 0.7$, and $\Omega_M = 0.3$.

2. OBSERVATIONS AND DATA REDUCTION

Observations were carried out using the LABOCA (Siringo et al. 2009) on the APEX telescope (Güsten et al. 2006) at Llano de Chajnantor in Chile. LABOCA is an array of 295 composite bolometers with neutron-transmutation-doped (NTD) germanium thermistors. The bolometers are AC-biased and operated in total power mode. Real-time signal processing of the 1 kHz data stream includes digital anti-alias filtering and down-sampling to 25 Hz. The radiation is coupled onto the detectors through an array of conical feed horns whose layout leads to a double beam spaced distribution of the individual beams in a hexagonal configuration over the 11.′4 field of view. The center wavelength of LABOCA is 870 μm (345 GHz) and its passband has an FWHM of $\sim$150 μm (60 GHz). The measured angular resolution of each beam is 19.″2 FWHM.

The observations[16] were carried out between 2007 May and 2008 November in mostly excellent weather conditions with an average precipitable water vapor (PWV) of 0.5 mm corresponding to a zenith opacity of 0.2 at the observing wavelength. The mapping pattern was chosen to give a uniform coverage across a $30' \times 30'$ area centered at R.A. $03^{\rm h}32^{\rm m}29.^{\rm s}0$, decl. $-27^{\circ}48'47.''0$. Mapping was performed by alternating rectangular, horizontal on-the-fly (OTF) scans with a raster of

[16] Program IDs 078.F-9028(A), 079.F-9500(A), 080.A-3023(A), and 081.F-9500(A).

spirals pattern. OTF maps were done with a scanning velocity of 2 arcmin s^{-1} and a spacing orthogonal to the scanning direction of 1′. For the spiral mode, the telescope traces in two scans spirals with radii between 2′ and 3′ at 16 and 9 positions (the raster) spaced by 10′ in azimuth and elevation (see Figure 9 in Siringo et al. 2009 for a plot of this scanning pattern). The radii and spacings of the spirals were optimized for uniform noise coverage across the 30′ × 30′ region, while keeping telescope overheads at a minimum. The scanning speed varies between 2 and 3 arcmin s^{-1}, modulating the source signals into the useful post-detection frequency band (0.1–12.5 Hz) of LABOCA, while providing at least three measurements per beam at the data rate of 25 samples per second even at the highest scanning velocity.

Absolute flux calibration was achieved through observations of Mars, Uranus, and Neptune as well as secondary calibrators (V883 Ori, NGC 2071 and VY CMa) and was found to be accurate within 8.5% (rms). The atmospheric attenuation was determined via skydips every ∼2 hr as well as from independent data from the APEX radiometer which measures the line-of-sight water vapor column every minute (see Siringo et al. 2009, for a more detailed description). Focus settings were typically determined a few times per night and checked during sunrise depending on the availability of suitable sources. Pointing was checked on the nearby quasars PMNJ0457-2324, PMNJ0106-4034, and PMNJ0403-3605 and found to be stable within 3″ (rms).

The data were reduced using the Bolometer array data Analysis software (BoA; F. Schuller et al. 2009, in preparation). Reduction steps on the time series (time-ordered data of each bolometer) include temperature drift correction based on two "blind" bolometers (whose horns have been sealed to block the sky signal), flat fielding, calibration, opacity correction, flagging of unsuitable data (bad bolometers and/or data taken outside reasonable telescope scanning velocity and acceleration limits) as well as de-spiking. The correlated noise removal was performed using the median signal of all bolometers in the array as well as on groups of bolometers related by the wiring and in the electronics (see Siringo et al. 2009). After the de-correlation, frequencies below 0.5 Hz were filtered using a noise whitening algorithm. Dead or noisy bolometers were identified based on the noise level of the reduced time series for each detector. The number of useful bolometers is typically ∼250. The data quality of each scan was evaluated using the mean rms of all useful detectors before correcting for the atmospheric attenuation (which effectively measures the instrumental noise equivalent flux density (NEFD)) and based on the number of spikes (measuring interferences). After omitting bad data we are left with an on-source integration time of ∼200 hr. Each good scan was then gridded into a spatial intensity and a weighting map with a pixel size of 6″ × 6″. This pixel size (∼1/3 of the beam size) well oversamples the beam and therefore accurately preserves the spatial information in the map. Weights are calculated based on the rms of each time series contributing to a certain grid point in the map. Individual maps were coadded noise-weighted. The resulting map was used in a second iteration of the reduction to flag those parts of the time streams with sources of a signal-to-noise ratio (S/N) $>3.7\sigma$. This cutoff is defined by our source extraction algorithm. The reduction with the significant sources flagged guarantees that the source fluxes are not affected by filtering and baseline subtraction and essentially corresponds to the very same reduction steps that have been performed on the calibrators.

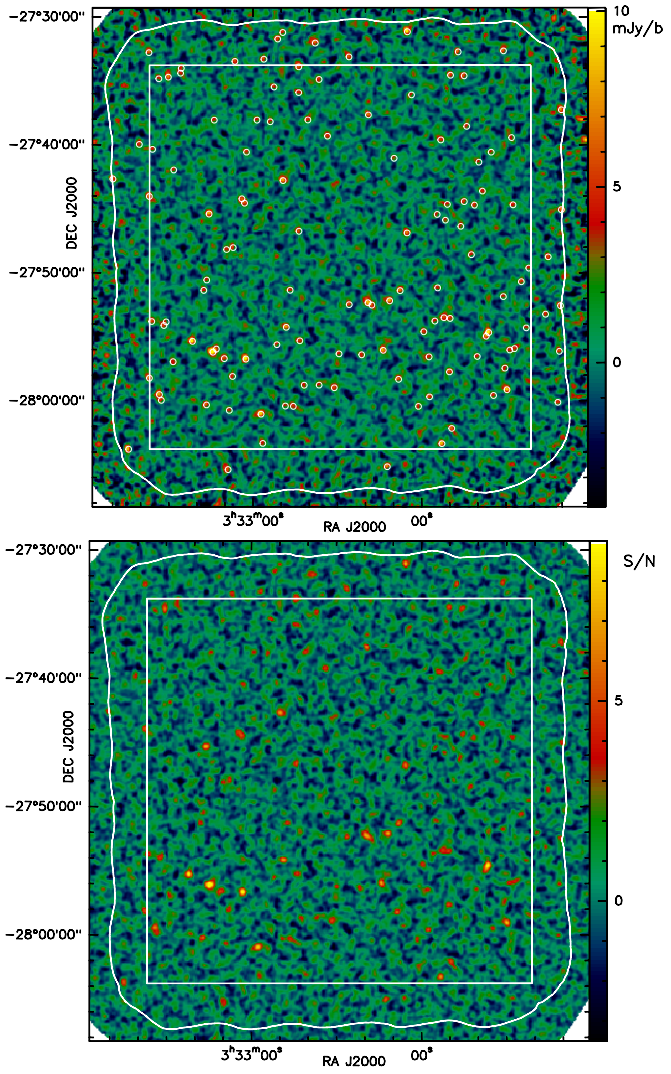

Figure 1. Flux (top) and signal-to-noise (bottom) map of the ECDFS at a spatial resolution of 27″ (beam smoothed). The white box shows the full 30′ × 30′ of the ECDFS as defined by the GEMS project. The white contour shows the 1.6 mJy $beam^{-1}$ noise level that has been used to define the field size for source extraction yielding a search area of 1260 $arcmin^2$. The circles in the top panel indicate the location of the sources listed in Table 1.

(A color version of this figure is available in the online journal.)

To remove remaining low-frequency noise artifacts we convolved the final coadded map with a 90″ Gaussian kernel and subtracted the resulting large-scale structures (LSSs) from the unsmoothed map. The convolution kernel has been adjusted to match the low-frequency excess in the map. This step is effectively equivalent to the low-frequency behavior of an optimal point-source (Wiener) filtering operation (Laurent et al. 2005). The effective decrease of the source fluxes (∼5%) for this well-defined operation has been taken into account by scaling the fluxes accordingly. Finally the map was beam smoothed (convolved by the beam size of 19.″2) to optimally filter the high frequencies for point sources. This step reduces the spatial resolution to ≈27″. The signal and signal to noise presentations of our final data product is shown in Figure 1.

To ensure that above reduction steps do not affect the flux calibration of our map, we performed the same reduction steps on simulated time streams with known source fluxes and artificial correlated and Gaussian noise. These tests verified that

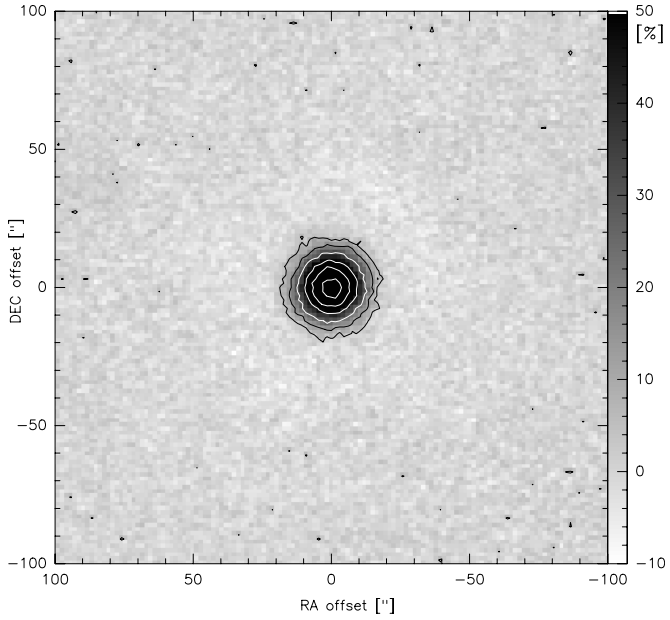

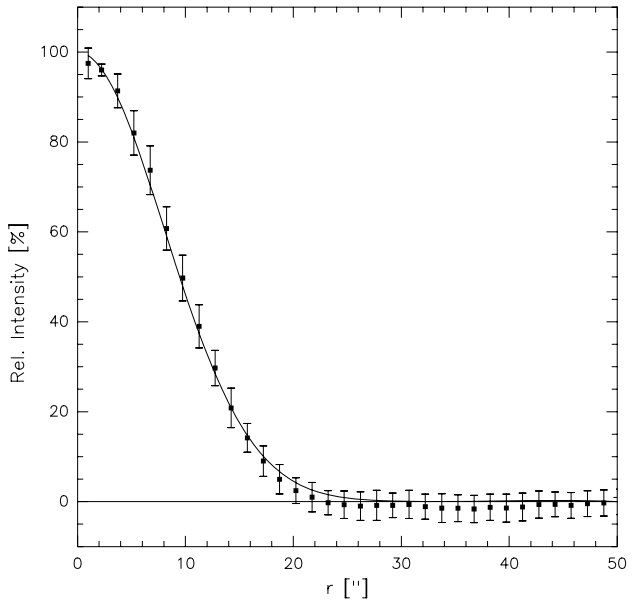

Figure 2. Top: normalized flux map of PMNJ0403-3605 (flux 590 mJy), the most frequently used pointing source near the ECDFS, reduced in the same way as the ECDFS scans. Contours are shown at 5%, 15% (black) and 30%, 50%, 70%, and 90% (white) of the peak flux density. Bottom: radial averaged beam profile. The solid line shows a Gaussian fit that yields an FWHM of 19.″2.

our calibration scheme is accurate to ∼5%. Furthermore we reduced data of PSS 2322+1944, a $z = 4.1$ QSO which has been observed during the science verification of LABOCA, in the same way as the ECDFS data. From this measurement we find $S_{870\,\mu m} = 21.1 \pm 2.5$ mJy in good agreement with the SCUBA measurements (22.5 ± 2.5 mJy; Isaak et al. 2002).

Finally we determined the point-spread function (PSF) in our map by applying the same data reduction steps to PMNJ0403-3605, the most frequently used pointing source near the ECDFS. The beam profile (before beam smoothing) is shown in Figure 2 and is well described by a Gaussian with an FWHM of 19.″2. The faint negative structure at radii between 25″ and 45″ is due to the combined effect of the correlated noise removal, the low-frequency filtering on the time series, and the spatial large scale filtering.

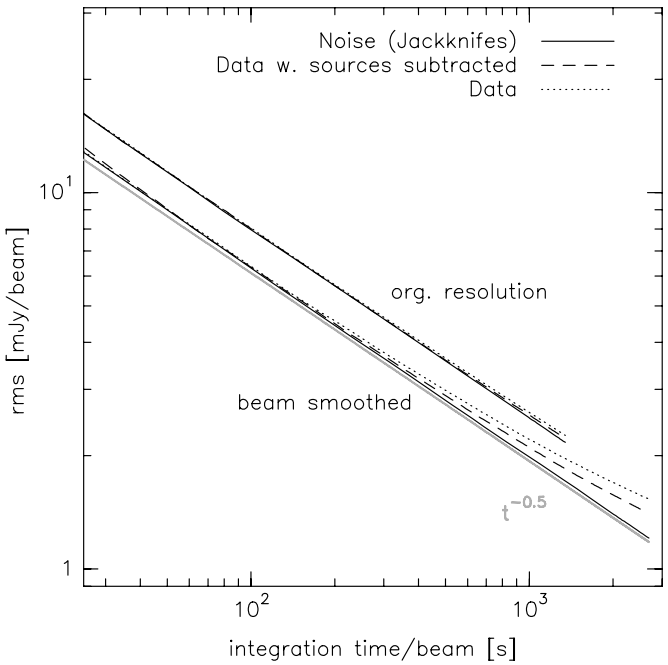

Figure 3. Average noise level in the ECDFS as a function of integration time. The upper lines represent the unsmoothed data at a spatial resolution of 19.″2. The three lines show the rms noise vs. integration time for the pure noise maps (jackknifes—solid line), the flux map after subtraction of all sources in the catalog (see Section 3.2.4—dashed line) and for the flux map including all sources (dotted line). The lower curves are the same but for beam-smoothed data (27.″2 spatial resolution). The gray solid line has a slope of −0.5 and shows the expected behavior for pure noise.

3. RESULTS

3.1. Noise Properties

To investigate the noise properties of our LABOCA map we have created 100 pure noise realizations of the data by randomly inverting half of the maps of individual scans during the coadding (e.g., Perera et al. 2008; Scott et al. 2008). All image processing steps match the real map including the large-scale filtering. These so-called "jackknife maps" are therefore free of any astronomical signal and at the same time represent the noise structure of the data.

We first investigate how the noise in our map integrates down with time. This is shown in Figure 3 where we plot the rms noise level measured on the central $30' \times 30'$ of our map as a function of the integration time per beam. We have generated down-integration curves for the pure noise realizations, the unmodified data, and for the data after subtracting the full source catalog (see Section 3.2.4) from each scan. All three computations were done at the original spatial resolution as well as for the beam-smoothed data. Ten computations with randomized scan order were performed for each method. Figure 3 shows the average of these computations.

As expected, the pure noise realizations integrate down proportionally to $\sqrt{1/t}$ independent of the spatial resolution. At an original spatial resolution of 19.″2, the influence of the source signals is small and even the down-integrating of the data including all sources follows this behavior very closely. Some excess noise is barely visible after several hundred seconds of integration time per beam. The noise excess becomes very pronounced for the beam-smoothed data and it remains visible even after the subtraction of the source catalog from the data. In fact, much of the noise access (65%) remains in our beam-

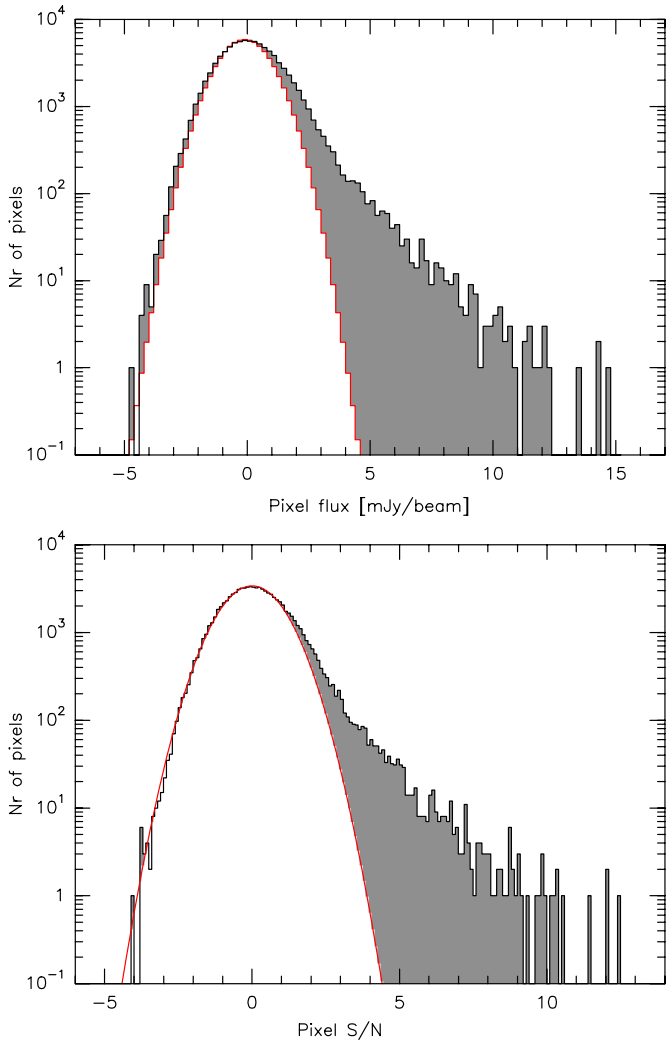

Figure 4. Top: observed beam-smoothed flux histogram (black) compared to the average flux histogram of the 100 jackknifes (normalized to the same peak) in the ECDFS. The positive access is due to sources, and the broadening of the negative part of the observed flux histogram is due to the confusion noise (see text). Bottom: beam-smoothed signal-to-noise histogram computed from the scaled weights of the map resulting in a Gaussian with $\sigma = 1$ (see Section 3.1). (A color version of this figure is available in the online journal.)

smoothed down-integrating curves after source subtraction. This shows that the noise in our map is limited by sources fainter than our catalog limit (∼4.7 mJy; Section 3.2.4) or in other words that our map starts to be confusion limited. We have estimated the confusion noise arising from these faint sources by fitting the down integration curve for the beam-smoothed data using

$$\sigma_{\rm obs}(t) = \sqrt{\sigma_{\rm n}^2(t) + \sigma_c^2}, \quad (1)$$

where $\sigma_{\rm obs}$, $\sigma_{\rm n}$, and $\sigma_{\rm c}$ are the observed, instrumental/atmospheric and confusion noise terms, respectively. From this fit, we derive a confusion noise of $\sigma_{\rm c} \approx 0.9\,{\rm mJy\,beam^{-1}}$ at 27″ resolution. We note that this level of confusion noise is consistent with the simulated down-integration curves based on our source counts (see Section 3.3.1).

Given that our map rms is affected by confusion noise, the question arises which noise level is appropriate for computing the noise distribution across the field and the corresponding signal-to-noise map, which is used for source extraction. Usually, the weights of the data (reflecting the rms-weighted

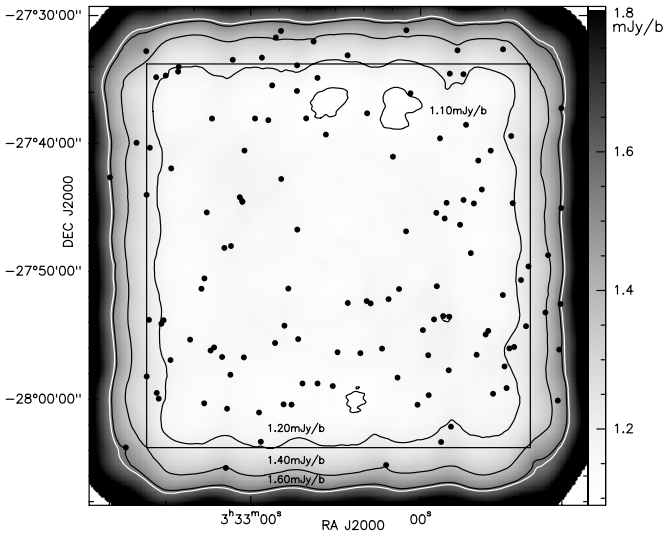

Figure 5. Noise map of the ECDFS at 27″ resolution (beam smoothed). The circles show the location of the 126 sources listed in Table 1. The black box shows the full 30′ × 30′ of the ECDFS. The white contour shows the field size that was used for source extraction. The black contours show the noise level at 1.1, 1.2, 1.4, and 1.6 mJy beam^{-1}.

integration time in each pixel) are used to derive the noise distribution. This approach, however, is equivalent to using the jackknife noise, neglects the confusion noise and therefore overestimates the S/N. We here use the noise based on the weights with a scaling to take the confusion noise into account. The scaling was determined from the flux and signal-to-noise histograms in the ECDFS. The basic principle is shown in Figure 4 (top) where we compare the average beam-smoothed flux pixel histograms of the jackknifes to a histogram of the real map. The figure shows that the negative part of the observed histogram is significantly broader than the jackknife histogram. This is because inserting sources in a pure noise map (e.g., the jackknife) will not only result in the positive flux tail, but also shift the entire flux histogram to positive values and broaden the Gaussian part of the distribution (because it is no longer centered around zero and sources also fall on the formally negative part of the flux distribution). As the zero point (true total power information) is undetermined in our reduction (e.g., via baseline subtraction), the observed flux histogram is roughly centered at zero and only the broadening remains an observable compared to the jackknife. This broadening can be used to take the confusion noise into account. In practice, we have scaled the rms map derived from the weights such that the negative part of the Gaussian signal-to-noise histogram (Figure 4, bottom panel) has a σ of unity.

The resulting spatial distribution of the beam-smoothed noise level across the imaged field is shown in Figure 5. The deepest part of our map has a noise level of 1.10 mJy beam^{-1}, the typical rms at the edges of the 30′ × 30′ field is 1.25 mJy beam^{-1}. The average noise level across the field is 1.17 mJy beam^{-1} with a dispersion of 40 μJy beam^{-1} only. For comparison with previous work we compare the area and the noise level of selected millimeter/submillimeter deep field survey to the LESS in Figure 6.

3.2. Source Catalog

3.2.1. Source Extraction Algorithm

From the beam-smoothed map we have extracted sources using the false detection rate (FDR) algorithm (for a description of

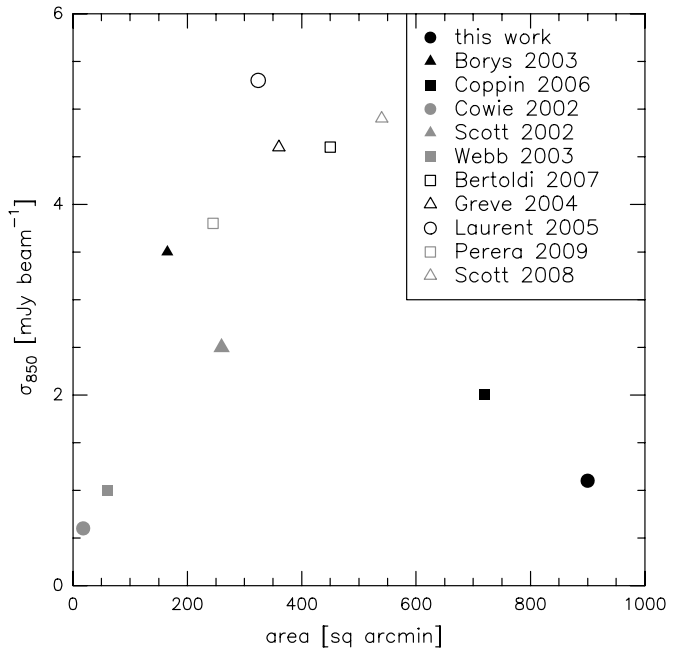

Figure 6. Area and mean 850 μm noise level for selected millimeter/submillimeter deep fields compared to LESS. Filled and open symbols represent 850 μm and 1.1 mm surveys, respectively. For the latter we have scaled the noise level by a factor of 3.8, the mean flux ratio of SMGs between both wavelengths (Greve et al. 2008).

this method see, e.g., Hopkins et al. 2002) of the CRUSH package (Kovács 2008). The choice of beam smoothing becomes obvious if one considers the maximum likelihood amplitude A of a point source (i.e., the beam B) fitted at a given position $\mathbf{x}$ in the map $S(\mathbf{x})$. Consider a weighted χ^2 of the fit defined in the usual way as

$$\chi^2 = \sum_{\mathbf{x}'} w(\mathbf{x}')[S(\mathbf{x}') - A(\mathbf{x})B(\mathbf{x} - \mathbf{x}')]^2. \quad (2)$$

Then, the χ^2 minimizing condition $\partial\chi^2/\partial A = 0$ yields a maximum likelihood amplitude:

$$A(\mathbf{x}) = \frac{\sum_{\mathbf{x}'} w(\mathbf{x}')B(\mathbf{x} - \mathbf{x}')S(\mathbf{x}')}{\sum_{\mathbf{x}'} w(\mathbf{x}')B^2(\mathbf{x} - \mathbf{x}')}, \quad (3)$$

which is effectively the weighted beam-smoothed image. Thus, the flux values of the beam-smoothed map essentially measure the fitted beam amplitudes at each map position (see also Serjeant et al. 2003; Gawiser et al. 2006).

The algorithm uses as in input parameter the allowed number of false detections. Based on this number and the field/beam size we calculate as an initial search criterion a detection signal-to-noise cutoff level assuming Gaussian noise statistics. When identifying source candidates, we allow for the possibility that the true peak may fall between pixels by appropriately relaxing the initial search S/N. Then for each source candidate, we interpolate the neighboring pixel values to estimate the underlying peak and its position, and keep only candidates that meet the original detection S/N level. We also apply the same procedure to identify negative noise peaks. These we use to check if the FDR is consistent with Gaussian noise, or to adjust the empirical noise distribution for possible deviations thereof.

The source candidates thus identified are removed from the map using the appropriate LSS-filtered beam profiles. LSS filtering corrections are also calculated for each pair of source candidates. The maps are flagged around the extracted source positions. After the extraction step, the zero flux level of the map is re-estimated via the mode of the pixel distribution (which we consider the most robust measure in this case). We also re-estimate the width of the noise distribution using robust measures. The extraction steps are repeated until no further candidates are identified.

For each candidate, we calculate a detection probability based on the number of sources detected beforehand and of the number noise peaks found (or expected) below the corresponding inverted significance level, under the assumption of a symmetric noise probability distribution. Finally, the candidates are sorted in order of decreasing detection probability. For each source we indicate the corresponding cumulative FDR in Table 1.

3.2.2. Completeness and Position Accuracy

To test the reliability of our extraction process and to obtain information on the completeness of our catalog we ran our extraction algorithm on 100 jackknife noise realizations after inserting artificial sources. The sources were added at random positions for each jackknife map and therefore represent an unclustered source population. For the source flux distribution we used a power law consistent with the differential source counts derived in Section 3.3. Simulated sources were inserted down to a flux level of 1.0 mJy, i.e., well below our detection threshold for individual source. The total number of simulated sources per jackknife map was ~6000. The large number of sources implies that the effect of confusion noise is taken into account in our extraction. The completeness computed from these simulations is shown in the middle panel of Figure 7. The figure shows that our source extraction is complete (>95%) down to an input source flux of ~6.5 mJy while the 50% completeness level occurs at ~4.0 mJy.

We also used our Monte Carlo simulations to estimate the accuracy of the source coordinates determined by our source extraction algorithm. This is shown in the top panel of Figure 7, where we plot the positional difference between input and extracted position as a function of the measured S/N of the extracted sources. The mean positional uncertainty is in good agreement with Equation (B22) from Ivison et al. (2007; red line). The scatter in the low-S/N bins (<5), however, is large which implies that the positional uncertainties from above equation are only correct in a statistical sense and that the true offset of an individual source can be much larger. From the simulations we find that for our extraction limit (S/N > 3.7) >95% of the sources will have a positional accuracy better than 8″. For the brightest sources (S/N > 7) the 95% confidence radius is ≈3.″5.

We note that because of the large number of independent observations in our map the telescope pointing accuracy will not affect the astrometry of our sources but result in a small (<3%) spatial smearing of their signals. The accuracy of the absolute astrometry of our map has been tested based on our stacking analysis of a sample of near-IR selected galaxies (Greve et al. 2009). These stacks give signals with up to 20σ significance centered on the expected position for different K-band-selected source populations and result in signal profiles in agreement with the beam shape. From this we conclude that there is no evidence for an overall mean astrometric error of our data. This is also confirmed by a comparison of the 1.4 GHz radio relative to the submillimeter positions (A. Biggs et al. 2009, in preparation).

Table 1
870 μm LABOCA Source Catalog of the ECDFS

Name (IAU)	R.A. J2000.0	Decl. J2000.0	$S_{\nu\,\mathrm{obs}}$ (mJy)	[a] $S_{\nu\,\mathrm{deboost}}$ (mJy)	S/N	[b]FDR	[c]Remark
LESS J033314.3–275611	03 33 14.26	−27 56 11.2	14.7 ± 1.2	14.5 ± 1.2	12.5	0.0	1,2
LESS J033302.5–275643	03 33 02.50	−27 56 43.6	12.2 ± 1.2	12.0 ± 1.2	10.3	0.0	1,2
LESS J033321.5–275520	03 33 21.51	−27 55 20.2	11.9 ± 1.2	11.7 ± 1.2	10.1	0.0	1,2
LESS J033136.0–275439	03 31 36.01	−27 54 39.2	11.2 ± 1.2	11.0 ± 1.2	9.7	0.0	1,2
LESS J033129.5–275907	03 31 29.46	−27 59 07.3	10.1 ± 1.2	10.0 ± 1.2	8.5	0.0	1,2
LESS J033257.1–280102	03 32 57.14	−28 01 02.1	9.8 ± 1.2	9.7 ± 1.2	8.2	0.0	1,2
LESS J033315.6–274523	03 33 15.55	−27 45 23.6	9.4 ± 1.2	9.2 ± 1.2	7.9	0.0	1,2
LESS J033205.1–273108	03 32 05.07	−27 31 08.8	12.1 ± 1.6	11.7 ± 1.6	7.8	0.0	1,2
LESS J033211.3–275210	03 32 11.29	−27 52 10.4	9.4 ± 1.2	9.2 ± 1.2	7.7	0.0	1,2
LESS J033219.0–275219	03 32 19.02	−27 52 19.4	9.3 ± 1.2	9.1 ± 1.2	7.6	0.0	1,2
LESS J033213.6–275602	03 32 13.58	−27 56 02.5	9.2 ± 1.2	9.1 ± 1.2	7.6	0.0	1,2
LESS J033248.1–275414	03 32 48.12	−27 54 14.7	8.9 ± 1.2	8.8 ± 1.2	7.2	0.0	1,2
LESS J033249.2–274246	03 32 49.23	−27 42 46.6	8.9 ± 1.2	8.8 ± 1.2	7.2	0.0	1,2
LESS J033152.6–280320	03 31 52.64	−28 03 20.4	9.5 ± 1.3	9.3 ± 1.3	7.2	0.0	1,2
LESS J033333.4–275930	03 33 33.36	−27 59 30.1	9.1 ± 1.3	8.9 ± 1.3	7.0	0.0	1,2
LESS J033218.9–273738	03 32 18.89	−27 37 38.7	8.2 ± 1.2	8.1 ± 1.2	6.9	0.0	1,2
LESS J033207.6–275123	03 32 07.59	−27 51 23.0	7.8 ± 1.2	7.6 ± 1.3	6.4	0.0	1
LESS J033205.1–274652	03 32 05.12	−27 46 52.1	7.7 ± 1.2	7.5 ± 1.2	6.3	0.0	1,2
LESS J033208.1–275818	03 32 08.10	−27 58 18.7	7.5 ± 1.2	7.3 ± 1.2	6.2	0.0	2
LESS J033316.6–280018	03 33 16.56	−28 00 18.8	7.5 ± 1.2	7.2 ± 1.2	6.2	0.0	1
LESS J033329.9–273441	03 33 29.93	−27 34 41.7	7.9 ± 1.3	7.6 ± 1.3	6.1	0.0	2
LESS J033147.0–273243	03 31 47.02	−27 32 43.0	8.5 ± 1.4	8.0 ± 1.5	5.9	0.0	1,2
LESS J033212.1–280508	03 32 12.11	−28 05 08.5	8.8 ± 1.5	8.2 ± 1.5	5.9	0.0	1,2
LESS J033336.8–274401	03 33 36.79	−27 44 01.0	7.8 ± 1.3	7.4 ± 1.4	5.9	0.0	2
LESS J033157.1–275940	03 31 57.05	−27 59 40.8	7.0 ± 1.2	6.7 ± 1.3	5.8	0.0	1
LESS J033136.9–275456	03 31 36.90	−27 54 56.1	6.8 ± 1.2	6.6 ± 1.2	5.8	0.0	1
LESS J033149.7–273432	03 31 49.73	−27 34 32.7	7.6 ± 1.3	7.2 ± 1.4	5.8	0.0	1
LESS J033302.9–274432	03 33 02.92	−27 44 32.6	7.0 ± 1.3	6.7 ± 1.3	5.6	0.0	1,2
LESS J033336.9–275813	03 33 36.90	−27 58 13.0	7.6 ± 1.4	7.1 ± 1.4	5.6	0.0	1
LESS J033344.4–280346	03 33 44.37	−28 03 46.1	9.7 ± 1.7	8.7 ± 1.8	5.6	0.0	2
LESS J033150.0–275743	03 31 49.96	−27 57 43.9	6.7 ± 1.2	6.3 ± 1.3	5.5	0.0	1,2
LESS J033243.6–274644	03 32 43.57	−27 46 44.0	6.8 ± 1.2	6.4 ± 1.3	5.5	0.0	1
LESS J033149.8–275332	03 31 49.78	−27 53 32.9	6.8 ± 1.3	6.4 ± 1.3	5.5	0.0	0
LESS J033217.6–275230	03 32 17.64	−27 52 30.3	6.8 ± 1.3	6.3 ± 1.3	5.4	0.0	0
LESS J033110.4–273714	03 31 10.35	−27 37 14.8	9.1 ± 1.7	8.1 ± 1.8	5.4	0.0	2
LESS J033149.2–280208	03 31 49.15	−28 02 08.7	6.9 ± 1.3	6.4 ± 1.4	5.4	0.0	2
LESS J033336.0–275347	03 33 36.04	−27 53 47.6	7.3 ± 1.4	6.7 ± 1.5	5.3	0.0	0
LESS J033310.2–275641	03 33 10.20	−27 56 41.5	6.4 ± 1.2	6.0 ± 1.3	5.2	0.0	0
LESS J033144.9–273435	03 31 44.90	−27 34 35.4	6.8 ± 1.3	6.2 ± 1.4	5.2	0.0	0
LESS J033246.7–275120	03 32 46.74	−27 51 20.9	6.4 ± 1.2	5.9 ± 1.3	5.2	0.0	2
LESS J033110.5–275233	03 31 10.47	−27 52 33.2	8.7 ± 1.7	7.6 ± 1.9	5.2	0.0	1
LESS J033231.0–275858	03 32 31.02	−27 58 58.1	6.4 ± 1.2	5.8 ± 1.4	5.1	0.0	2
LESS J033307.0–274801	03 33 07.00	−27 48 01.0	6.4 ± 1.3	5.9 ± 1.4	5.1	0.0	0
LESS J033131.0–273238	03 31 30.96	−27 32 38.5	7.5 ± 1.5	6.7 ± 1.6	5.1	0.0	0
LESS J033225.7–275228	03 32 25.71	−27 52 28.5	6.3 ± 1.2	5.8 ± 1.4	5.1	0.0	1
LESS J033336.8–273247	03 33 36.80	−27 32 47.0	8.2 ± 1.6	7.2 ± 1.8	5.1	0.0	0
LESS J033256.0–273317	03 32 56.00	−27 33 17.7	7.0 ± 1.4	6.3 ± 1.5	5.1	0.0	0
LESS J033237.8–273202	03 32 37.77	−27 32 02.0	7.7 ± 1.5	6.8 ± 1.7	5.1	0.0	0
LESS J033124.5–275040	03 31 24.45	−27 50 40.9	6.6 ± 1.3	5.9 ± 1.4	5.1	0.0	1,2
LESS J033141.2–274441	03 31 41.15	−27 44 41.5	6.1 ± 1.2	5.6 ± 1.3	5.0	0.0	1,2
LESS J033144.8–274425	03 31 44.81	−27 44 25.1	6.2 ± 1.2	5.6 ± 1.3	5.0	0.0	2
LESS J033128.5–275601	03 31 28.51	−27 56 01.3	6.2 ± 1.3	5.6 ± 1.4	4.9	0.0	1
LESS J033159.1–275435	03 31 59.12	−27 54 35.5	6.2 ± 1.3	5.6 ± 1.4	4.9	0.0	2
LESS J033243.6–273353	03 32 43.61	−27 33 53.6	6.8 ± 1.4	6.0 ± 1.5	4.9	0.0	2
LESS J033302.2–274033	03 33 02.20	−27 40 33.6	6.1 ± 1.2	5.5 ± 1.4	4.9	0.0	0
LESS J033153.2–273936	03 31 53.17	−27 39 36.1	6.0 ± 1.2	5.4 ± 1.4	4.9	0.0	1
LESS J033152.0–275329	03 31 51.97	−27 53 29.7	6.1 ± 1.3	5.5 ± 1.4	4.9	0.0	0
LESS J033225.8–273306	03 32 25.79	−27 33 06.7	6.7 ± 1.4	5.9 ± 1.6	4.8	0.0	0
LESS J033303.9–274412	03 33 03.87	−27 44 12.2	6.0 ± 1.3	5.3 ± 1.4	4.8	0.0	0
LESS J033317.5–275121	03 33 17.47	−27 51 21.5	5.8 ± 1.2	5.2 ± 1.4	4.8	0.1	1
LESS J033245.6–280025	03 32 45.63	−28 00 25.3	5.9 ± 1.2	5.2 ± 1.4	4.7	0.1	0
LESS J033236.4–273452	03 32 36.41	−27 34 52.5	6.1 ± 1.3	5.4 ± 1.5	4.7	0.1	2
LESS J033308.5–280044	03 33 08.46	−28 00 44.3	6.0 ± 1.3	5.3 ± 1.4	4.7	0.1	2
LESS J033201.0–280025	03 32 01.00	−28 00 25.6	5.8 ± 1.2	5.1 ± 1.4	4.7	0.1	1
LESS J033252.4–273527	03 32 52.40	−27 35 27.7	5.9 ± 1.3	5.2 ± 1.4	4.7	0.1	0
LESS J033331.7–275406	03 33 31.69	−27 54 06.1	6.1 ± 1.3	5.3 ± 1.5	4.7	0.1	0

Table 1
(Continued)

Name (IAU)	R.A. J2000.0	Decl. J2000.0	$S_{\nu\,\mathrm{obs}}$ (mJy)	[a] $S_{\nu\,\mathrm{deboost}}$ (mJy)	S/N	[b] FDR	[c] Remark
LESS J033243.3–275517	03 32 43.28	−27 55 17.9	5.9 ± 1.3	5.2 ± 1.4	4.7	0.1	0
LESS J033233.4–273918	03 32 33.44	−27 39 18.5	5.8 ± 1.3	5.1 ± 1.4	4.7	0.1	1
LESS J033134.3–275934	03 31 34.26	−27 59 34.3	5.7 ± 1.2	5.0 ± 1.3	4.7	0.1	1
LESS J033144.0–273832	03 31 43.97	−27 38 32.5	5.7 ± 1.2	5.0 ± 1.4	4.6	0.1	2
LESS J033306.3–273327	03 33 06.29	−27 33 27.7	6.6 ± 1.4	5.6 ± 1.6	4.6	0.1	0
LESS J033240.4–273802	03 32 40.40	−27 38 02.5	5.7 ± 1.2	5.0 ± 1.4	4.6	0.1	1
LESS J033229.3–275619	03 32 29.33	−27 56 19.3	5.8 ± 1.3	5.1 ± 1.4	4.6	0.1	0
LESS J033309.3–274809	03 33 09.34	−27 48 09.9	5.8 ± 1.3	5.1 ± 1.4	4.6	0.1	0
LESS J033126.8–275554	03 31 26.83	−27 55 54.6	5.8 ± 1.3	5.1 ± 1.4	4.6	0.1	2
LESS J033332.7–275957	03 33 32.67	−27 59 57.2	6.0 ± 1.3	5.1 ± 1.5	4.5	0.1	0
LESS J033157.2–275633	03 31 57.23	−27 56 33.2	5.6 ± 1.3	4.8 ± 1.4	4.4	0.2	0
LESS J033340.3–273956	03 33 40.30	−27 39 56.9	6.2 ± 1.4	5.1 ± 1.7	4.4	0.3	1
LESS J033221.3–275623	03 32 21.25	−27 56 23.5	5.5 ± 1.3	4.7 ± 1.4	4.4	0.3	2
LESS J033142.2–274834	03 31 42.23	−27 48 34.4	5.4 ± 1.2	4.6 ± 1.4	4.4	0.3	2
LESS J033127.5–274440	03 31 27.45	−27 44 40.4	5.7 ± 1.3	4.8 ± 1.5	4.4	0.3	0
LESS J033253.8–273810	03 32 53.77	−27 38 10.9	5.4 ± 1.2	4.5 ± 1.4	4.4	0.3	0
LESS J033308.9–280522	03 33 08.92	−28 05 22.0	6.7 ± 1.5	5.3 ± 1.8	4.4	0.3	0
LESS J033154.2–275109	03 31 54.22	−27 51 09.8	5.5 ± 1.3	4.6 ± 1.4	4.3	0.4	0
LESS J033110.3–274503	03 31 10.28	−27 45 03.1	8.2 ± 1.6	6.0 ± 2.4	4.3	0.4	1
LESS J033114.9–274844	03 31 14.90	−27 48 44.3	6.5 ± 1.5	5.1 ± 1.8	4.3	0.4	0
LESS J033251.1–273143	03 32 51.09	−27 31 43.0	6.7 ± 1.6	5.3 ± 1.9	4.3	0.5	0
LESS J033155.2–275345	03 31 55.19	−27 53 45.3	5.4 ± 1.3	4.5 ± 1.4	4.3	0.5	0
LESS J033248.4–280023	03 32 48.44	−28 00 23.8	5.3 ± 1.2	4.4 ± 1.4	4.3	0.5	0
LESS J033243.7–273554	03 32 43.65	−27 35 54.1	5.4 ± 1.3	4.5 ± 1.5	4.2	0.6	0
LESS J033135.3–274033	03 31 35.25	−27 40 33.7	5.3 ± 1.3	4.4 ± 1.4	4.2	0.6	0
LESS J033138.4–274336	03 31 38.36	−27 43 36.0	5.2 ± 1.2	4.3 ± 1.4	4.2	0.6	0
LESS J033110.8–275607	03 31 10.84	−27 56 07.2	6.9 ± 1.7	5.2 ± 2.0	4.2	0.6	0
LESS J033307.3–275805	03 33 07.27	−27 58 05.0	5.3 ± 1.3	4.4 ± 1.4	4.2	0.7	0
LESS J033241.7–275846	03 32 41.74	−27 58 46.1	5.2 ± 1.3	4.3 ± 1.4	4.2	0.7	0
LESS J033313.0–275556	03 33 13.03	−27 55 56.8	5.2 ± 1.2	4.3 ± 1.4	4.2	0.7	0
LESS J033313.7–273803	03 33 13.65	−27 38 03.4	5.1 ± 1.2	4.2 ± 1.4	4.2	0.8	0
LESS J033130.2–275726	03 31 30.22	−27 57 26.0	5.1 ± 1.3	4.2 ± 1.4	4.1	1.0	0
LESS J033251.5–275536	03 32 51.45	−27 55 36.0	5.3 ± 1.3	4.3 ± 1.4	4.1	1.0	0
LESS J033111.3–280006	03 31 11.32	−28 00 06.2	6.4 ± 1.6	4.8 ± 1.9	4.1	1.0	0
LESS J033151.5–274552	03 31 51.47	−27 45 52.1	5.1 ± 1.3	4.2 ± 1.4	4.1	1.1	1
LESS J033335.6–274020	03 33 35.61	−27 40 20.1	5.4 ± 1.3	4.3 ± 1.5	4.1	1.2	0
LESS J033325.4–273400	03 33 25.35	−27 34 00.4	5.5 ± 1.3	4.3 ± 1.5	4.1	1.2	0
LESS J033258.5–273803	03 32 58.46	−27 38 03.0	4.9 ± 1.2	4.0 ± 1.4	4.1	1.3	0
LESS J033115.8–275313	03 31 15.78	−27 53 13.1	6.0 ± 1.5	4.6 ± 1.7	4.1	1.3	0
LESS J033140.1–275631	03 31 40.09	−27 56 31.4	4.9 ± 1.2	4.0 ± 1.4	4.0	1.4	2
LESS J033130.9–275150	03 31 30.85	−27 51 50.9	5.0 ± 1.3	4.0 ± 1.4	4.0	1.4	0
LESS J033316.4–275033	03 33 16.42	−27 50 33.1	5.0 ± 1.2	4.0 ± 1.4	4.0	1.5	0
LESS J033328.1–274157	03 33 28.08	−27 41 57.0	5.0 ± 1.3	4.0 ± 1.4	4.0	1.6	0
LESS J033122.6–275417	03 31 22.64	−27 54 17.2	5.3 ± 1.3	4.1 ± 1.5	4.0	1.8	0
LESS J033325.6–273423	03 33 25.58	−27 34 23.0	5.2 ± 1.3	4.1 ± 1.5	4.0	1.9	0
LESS J033249.3–273112	03 32 49.28	−27 31 12.3	6.5 ± 1.7	4.6 ± 2.0	4.0	2.0	0
LESS J033236.4–275845	03 32 36.42	−27 58 45.9	5.0 ± 1.3	3.9 ± 1.4	3.9	2.0	0
LESS J033150.8–274438	03 31 50.81	−27 44 38.5	4.9 ± 1.3	3.9 ± 1.4	3.9	2.4	0
LESS J033349.7–274239	03 33 49.71	−27 42 39.2	7.4 ± 1.6	4.6 ± 2.4	3.9	2.9	0
LESS J033154.4–274525	03 31 54.42	−27 45 25.5	4.9 ± 1.3	3.8 ± 1.4	3.8	3.0	0
LESS J033128.0–273925	03 31 28.02	−27 39 25.2	5.0 ± 1.3	3.8 ± 1.4	3.8	3.1	0
LESS J033121.8–274936	03 31 21.81	−27 49 36.8	5.2 ± 1.4	3.8 ± 1.5	3.8	3.7	0
LESS J033256.5–280319	03 32 56.51	−28 03 19.1	5.1 ± 1.4	3.8 ± 1.5	3.8	3.8	0
LESS J033328.5–275655	03 33 28.45	−27 56 55.9	4.9 ± 1.3	3.7 ± 1.5	3.8	3.8	0
LESS J033333.3–273449	03 33 33.32	−27 34 49.3	5.2 ± 1.4	3.8 ± 1.6	3.8	3.9	0
LESS J033139.6–274120	03 31 39.62	−27 41 20.4	4.7 ± 1.2	3.6 ± 1.5	3.8	4.0	0
LESS J033330.9–275349	03 33 30.88	−27 53 49.3	4.9 ± 1.3	3.7 ± 1.6	3.8	4.2	0
LESS J033203.6–273605	03 32 03.59	−27 36 05.0	4.6 ± 1.2	3.5 ± 1.4	3.7	4.7	0
LESS J033146.0–274621	03 31 46.02	−27 46 21.2	4.7 ± 1.3	3.6 ± 1.4	3.7	4.7	0
LESS J033209.8–274102	03 32 09.76	−27 41 02.0	4.7 ± 1.3	3.6 ± 1.4	3.7	4.9	0

Notes.

[a] De-boosted fluxes depend on the source count model (see Section 3.2.3) and are correct only in a statistical sense.

[b] Expected number of false detections for all sources including the corresponding entry in the table.

[c] The "Remark" entry indicates if a source is detected in the two submaps calculated by splitting the data into half (see Section 3.2.5). 1, 2: the source is detected in both submaps, 1 (2): the source is detected in submap 1 (2), 0: the source is not detected in any submap.

(This table is also available in a machine-readable form in the online journal.)

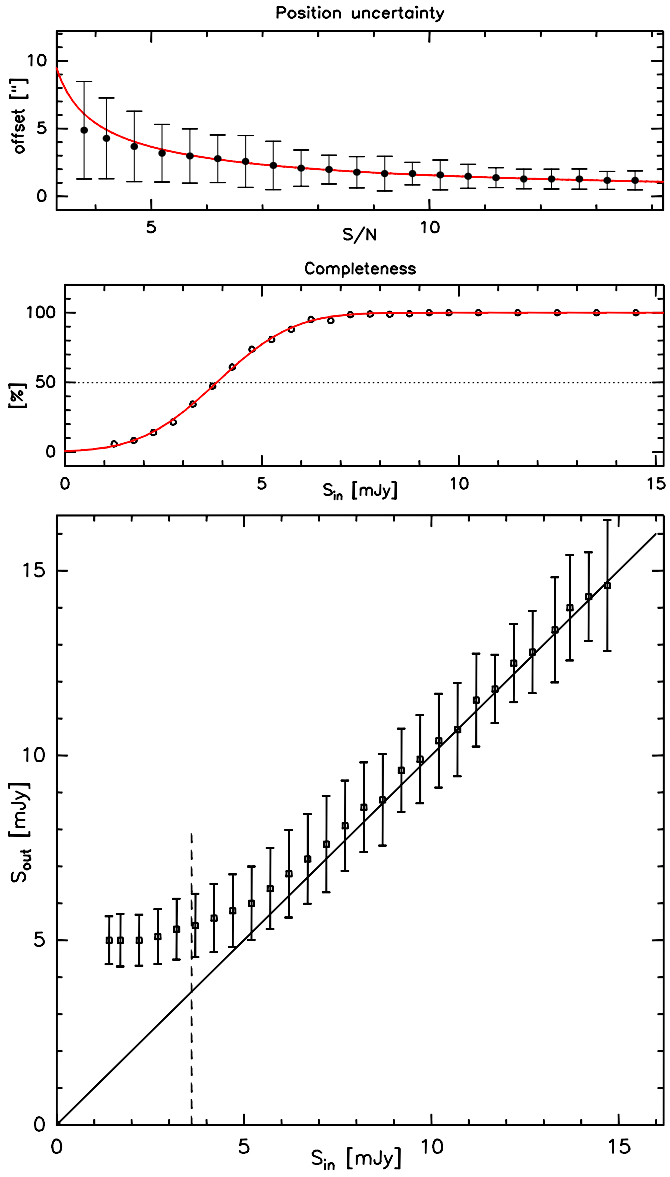

Figure 7. Top: position uncertainty as a function of observed S/N. Error bars show the rms of the extracted positions in each signal-to-noise bin, the red line shows the expected positional uncertainties using Equation (B22) from Ivison et al. (2007). Middle and bottom: completeness and flux boosting as a function of intrinsic source flux determined from Monte Carlo simulation. The dashed vertical line in the lower panel shows the lowest de-boosted flux in our source catalog.

(A color version of this figure is available in the online journal.)

3.2.3. Flux Boosting Correction

Signal-to-noise limited source catalogs carry a selection bias from an overabundance of sources whose apparent flux is positively enhanced by noise (e.g., Hogg & Turner 1998; Scott et al. 2002). This is shown in the bottom panel of Figure 7 where we compare the extracted flux densities to the input flux densities of our Monte Carlo simulations. The discrepancy between intrinsic fluxes and their detection values becomes noticeable below ∼6 mJy.

This effect arises because the steepness of submillimeter number counts implies that an observed flux $S_{\rm obs}$ more often arises from intrinsic fluxes $S < S_{\rm obs}$ and less often from $S > S_{\rm obs}$. The average flux value $\langle S\rangle$ behind an observed flux $S_{\rm obs}$ can be calculated statistically:

$$\langle S\rangle = \int Sp(S|S_{\rm obs})dS. \quad (4)$$

According to Bayesian theory, $p(S_i|S_{\rm obs}) \propto p(S_{\rm obs}|S)p(S)$. The probability density $p(S_{\rm obs}|S)$ of observing a flux $S_{\rm obs}$ for an underlying flux S is simply the noise distribution evaluated at the flux difference, i.e., $n(S - S_{\rm obs})$. For Gaussian noise $n(x)$ is calculated as $(\sigma\sqrt{2\pi})^{-1}\exp(-x^2/2\sigma^2)$. The term $p(S)$ is the probability density of flux S in the underlying noiseless flux distribution of the map, which accounts for the possibility of overlapping sources. As such, $p(S)$ is given by Equation (7) and is a direct product of our $P(D)$ analysis for the source number counts (see Section 3.3.1).

A slight complication arises because the map zeroing is biased by the presence of sources below detection level. If the map zero level corresponds to an intrinsic flux δS, then a map flux S really belongs to an underlying value $S + \delta S$. Fortunately, this δS is also readily produced by the $P(D)$ analysis. With the necessary modifications in place we can calculate de-boosted fluxes using

$$\langle S\rangle = \delta S + \frac{\int Sn(S - S_{\rm obs})p(S + \delta S)dS}{\int n(S - S_{\rm obs})p(S + \delta S)dS}. \quad (5)$$

The integration can be performed numerically. The corresponding uncertainty σ of the de-boosted flux can also be calculated as $\sigma^2 =< (S - \langle S\rangle)^2 >$, i.e., as

$$\sigma^2 = \frac{\int (S + \delta S - \langle S\rangle)^2 n(S - S_{\rm obs})p(S + \delta S)dS}{\int n(S - S_{\rm obs})p(S + \delta S)dS}. \quad (6)$$

The uncertainty of the de-boosted flux is typically larger than the measurement uncertainty. The effect is more pronounced at the lower fluxes.

To calculate the de-boosted fluxes for each source we have used $p(S)$ and δS from the single power-law fit from our $P(D)$ analysis derived in Section 3.3.1. Note that this is not an iterative process because the $P(D)$ fitting does not require information on the underlying counts.

3.2.4. The LESS Source Catalog

While our map has a uniform noise of 1.2 mJy beam^{-1} over 900 arcmin^2, an additional 360 arcmin^2 has only slightly higher noise, <1.6 mJy beam^{-1} (i.e., better than most previous surveys, see Figure 6), hence we expand our search area to allow us to find slightly brighter sources outside the uniform region (see Figure 1). To construct a robust catalog we restricted the extraction in such a way to give statistically five false detections. This yields a total of 126 sources that are listed in Table 1. The FDR of 5 implies a signal-to-noise cut above 3.7σ. The faintest sources in our catalog have measured flux densities of 4.6 mJy, at which level the completeness is >70% (Figure 7). In the table, we order the individual sources by their S/N and we give their IAU name, the source position, the measured source flux with the map noise as uncertainty, the de-boosted source flux and its uncertainty using a Bayesian approach (see Section 3.2.3), the S/N and the expected number of false detections for all sources including the corresponding entry in the table. From the last entry in the table it can be seen that only 10 additional sources are included in the catalog if we increase the FDR from 3 to 5 for the full catalog. This implies that 20% of the additional sources are likely to be false. Therefore deeper source extractions would not yield reliable information.

3.2.5. Tests on the LESS Source Catalog

To test the reliability of our source catalog we have compared the FDR from our Monte Carlo simulations to the FDR expectation for our source extraction algorithm. A source was considered to be detected if the extraction fell within a 8″ search radius (the maximum positional uncertainty expected for our extraction, see 3.2.2) from the input position. The FDRs derived in both ways agree very well with a slight tendency of our extraction algorithm to overestimate the FDR (for five expected false detections we find four from our Monte Carlo simulations).

To verify that our map does not contain false sources due to artifacts in the data or the data processing we split our observations into two parts. This was done by splitting the randomized scan list (2370 scans in total) into two lists with roughly equal integration time yields two independent maps with noise levels of ≈1.7 mJy beam^{-1}. We then performed our source extraction on both maps using the same significance level we used for the generation of our source catalog (3.7σ). This yields 59 and 60 extracted sources for map 1 and map 2, respectively which is in excellent agreement with the expected numbers considering the $\sqrt{2}$ increase of the noise level and the number counts derived from the full map.

From these extractions we find that 22 sources in the LESS catalog are detected in both submaps and that ∼70% of the sources extracted from both submaps are also in the LESS catalog. In the last entry of Table 1 we have indicated for each source of the LESS catalog whether they are detected in one, both, or none of the individual maps. Note that those sources extracted from both submaps which are not in the LESS catalog are not necessarily false detections as the different noise structure of the submap may boost other faint sources above the extraction threshold.

A comparison of the sources detected on maps 1 and 2 yields an overlap of both catalogs of ∼40%. For those sources that only appear in one of the two catalogs (37/38 for map 1/2) we have extracted the SNR peaks in a 8″ search radius on the map where the source is not detected and computed the probability that no source is present in this aperture. From this analysis we find that the probability of a false detection exceeds 10% for just 7(/6) source for submap 1(/2) which is in reasonable agreement with the five false detections expected from our extractions. We furthermore analyzed the stacked signal at the positions of the non-detections. For this we used the method described by Greve et al. (2009) which yields ≈12σ detections for both submaps with an average flux density of 3.5 ± 0.3 mJy for all positions and 4.3 ± 0.35 mJy if we exclude the 7(/6) false detections.

Finally we have investigated the stacked signal in maps 1 and 2 at each position at which a source is extracted in the LESS catalog, but not in both submaps. Again the stacked signals in both submaps give very similar results with ≈20σ detections and an average flux of 4.2 ± 0.2 mJy. The intensity of stacked signals is in good agreement with the mean de-boosted source flux of the LESS sources entering into the stack for both maps. These tests show that our FDR extraction yields reasonable results and that the average fluxes of the faint sources in the LESS catalog can be reproduced in the stacking signals of two independent submaps.

3.3. Differential Source Counts

Most studies that have addressed millimeter/submillimeter number counts from deep-field surveys have used the extracted sources, e.g., the resulting source catalogs to fit models to the differential or integrated number counts as a function of flux density (e.g., Barger et al. 1999; Blain et al. 1999; Scott et al. 2002; Greve et al. 2004; Coppin et al. 2006; Knudsen et al. 2008; Perera et al. 2008; Austermann et al. 2009). This approach relies on the correct determination of the completeness as well as on the flux de-boosting in order to extract the required information. In particular, the latter step is problematic because the de-boosting itself requires information on the underlying source count distribution (see, e.g., Coppin et al. 2005). Furthermore, blank field surveys contain also information on sources fainter than the typical cutoff levels used to extract sources (e.g., Peacock et al. 2000). This is shown for our LABOCA data in Figure 8 where we show the flux pixel histogram after subtracting all sources in our source catalog from the map. The diagram shows a significant access of pixels with positive flux densities which is due to sources below our source extraction limit. The increasing number of noise peaks at the same flux density level prevents an extraction directly from the map without increasing significantly the number of false detections in the analysis. One may, however, ignore the position information completely and derive the underlying source count distribution directly from the flux pixel histogram through a $P(D)$ analysis (see, e.g., Condon 1974; Hughes et al. 1998; Maloney et al. 2005). In the bottom panel of Figure 8, we show the pixel histogram of the positive excess after subtracting a Gaussian noise distribution. The latter has been determined by a fit to the negative part of the flux histogram. The errors in the figure are 3σ Poisson uncertainties. From the figure it can be seen that the excess becomes significant for flux densities above ∼1.5 mJy which implies that the source count distribution can be extracted to a much fainter level than the limits inherent to the source extraction method.

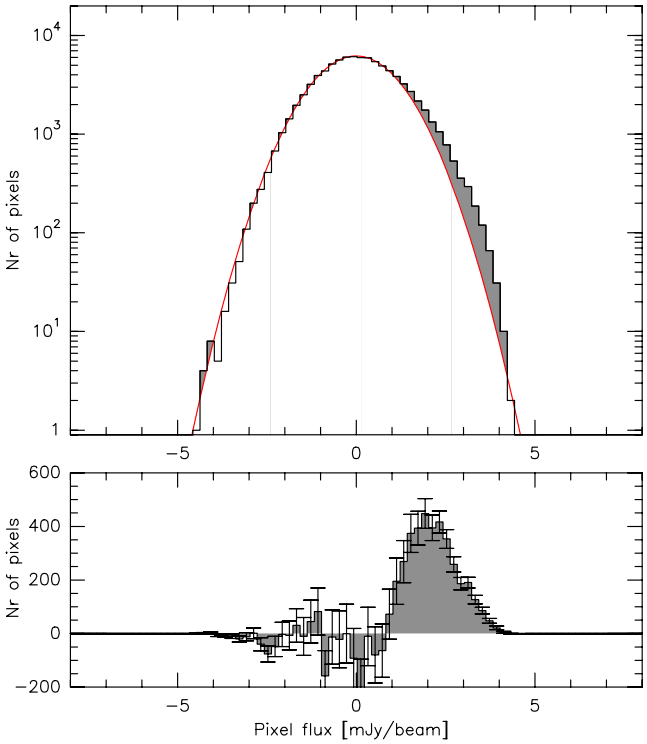

Figure 8. Top: histogram of the flux density distribution of all pixels in the central 30′ × 30′ after subtracting all sources from our catalog (Table 1). The curve represents a Gaussian fit to the underlying noise histogram fitted between −5.0 and 1.0 mJy. The region shows the residual positive access. Bottom: linear presentation of the flux excess. Errors are 3σ Poisson uncertainties.

(A color version of this figure is available in the online journal.)

3.3.1. $P(D)$ Analysis

Our approach is to directly use the information from the observed flux distribution in our map. Were there just a single source with flux S present at some random location in a noiseless map, it would give rise to a probability distribution $P(y|S)$ of pixel values y. If the map contains several such randomly distributed sources with fluxes $S_1 ... S_n$, then the probability $P(y|S_1 ... S_n)$ of observing a value y (in flux or S/N) can be related to the individual probability distributions $P(y|S_i)$ arising from each individual source and the measurement noise distribution $n(y)$ as

$$P(y|S_1 ... S_n) = P(y|S_1) \otimes ... \otimes P(y|S_n) \otimes n(y), \quad (7)$$

which simply follows the compounding rule for independent random variables via convolution. As such, it can be rewritten as the product of the complex Fourier transforms ($P \rightleftharpoons \pi$, and of $n \rightleftharpoons \nu$) of the distributions: $\pi(S_1 ... S_n) = \pi(S_1) \cdot \pi(S_2) ... \pi(S_n) \cdot \nu$. For example, if one considers discrete bins i, each containing N_i sources with flux S_i, then the characteristic function π (i.e., the Fourier transform) of the compound distribution is

$$\pi = \nu \cdot \prod_i \pi(S_i)^{n_i}. \quad (8)$$

Therefore, if one has sufficient knowledge of the underlying noise distribution and the probability distributions due to individual sources, then the bin counts, n_i, can be determined from the observed pixel distribution with standard nonlinear χ^2-minimization techniques applied in the Fourier domain. The fitting must also include a parameter δS for the true underlying flux corresponding to map zero values. The differential source counts are directly proportional to the bin counts and are expressed as $dN/dS(S_i) = n_i/A\Delta_i$, in terms of the fitted map area A and the bin width Δ_i.

The pixel distributions arising from sources relies on the knowledge of the PSF, which in our case is the closely Gaussian shape of the LABOCA beam (Figure 2), which has been smoothed and large-scale filtered exactly like the input map. The underlying noise distribution was obtained directly from the jackknifed maps (Section 3.1), which were also smoothed and large-scale filtered identically to the input map.

It is practical to apply the method on the signal-to-noise rather than the flux distribution of the map, as here the noise distribution is the narrowest when coverage is not uniform. This helps to limit the unwanted "smearing" of the analyzed probability distribution, thereby improving sensitivity for determining the underlying source counts. In our case, due to the highly uniform coverage in the central $30' \times 30'$ area of our map used for determining source counts, the choice between flux or signal-to-noise distribution fitting is less critical. Nevertheless, we analyzed the source counts on the beam-smoothed signal-to-noise image.

Our choice of a nonlinear fitting algorithm was based on the downhill simplex method (Press et al. 1986). To use high bin resolution, necessary given the expected steepness of the counts (e.g., Coppin et al. 2006), and at the same time limit the number of fitted parameters to a handful (in order to minimize covariances between them and to obtain precise fit values for each of these) we fitted common source-count laws rather than the individual bin counts n_i.

We have fitted four different source count models to the observed histogram: a single and a broken power law, a Schechter function, and a power law with constant counts at the faint end of the distribution as suggested by Barger et al. (1999). All models give comparable fits to the observed flux histogram with reduced χ^2 values about 1. The parameters for each model are given in Table 2. As only the Barger source count model yields finite counts for flux densities approaching zero, we also give the cutoff flux density derived from the fitting together with the implied total extragalactic 870 μm background light (EBL) contribution in the table. Figure 9 shows an example of the simulated flux histogram for the best-fitting Schechter function in comparison to the observations. Within the 3σ Poisson errors there is no significant difference between the model and the observations. The differential source counts are listed in Table 2 and are shown in Figure 10.

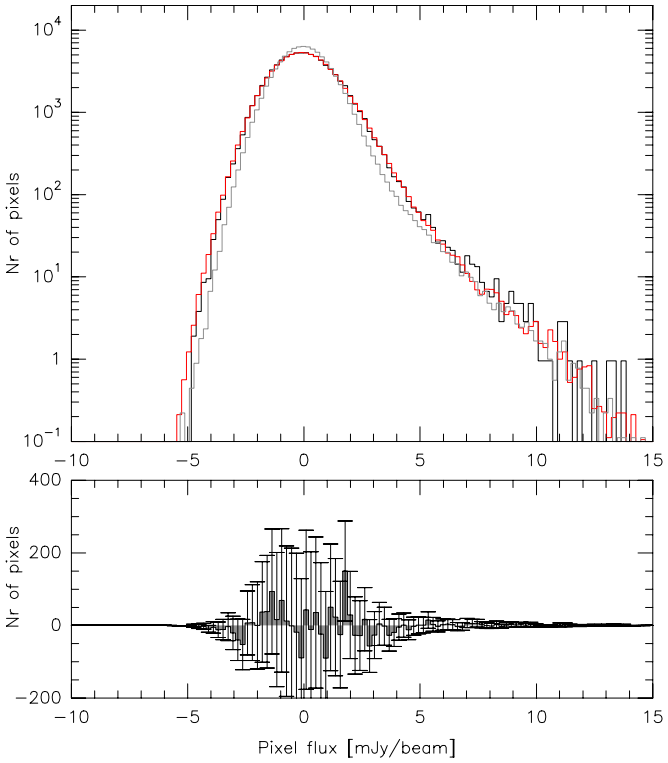

Figure 9. Top: logarithmic presentation of the observed flux density histogram (black) and fit results from the $P(D)$ analysis (red) in the central $30' \times 30'$ of the E-CDFS. Bottom: linear presentation of the residual between the observed and fitted flux density histogram. Errors are 3σ Poisson uncertainties. The gray histogram in the top panel shows for comparison the flux density distribution for a Schechter function as derived for the SHADES survey with N' matched to the LESS source counts (dashed gray line in Figure 10, left).

(A color version of this figure is available in the online journal.)

3.3.2. Direct Estimate of the Differential Source Counts

To compute the differential source counts directly from the source catalog, we have used an approach similar to that of Coppin et al. (2006). To determine the posterior flux density distribution for each source we have used the power-law function derived from our $P(D)$ analysis (Table 2) as a prior for the Bayesian de-boosting of the observed flux density. The differential source counts were calculated from the de-boosted fluxes taking the Gaussian likelihood that a source falls into a given flux bin as well as the completeness of this bin into account. The resulting differential source counts are shown together with the best-fitting models from our $P(D)$ analysis in Figure 10 (left). In the figure, we show for comparison the differential source counts from the SHADES survey (Coppin

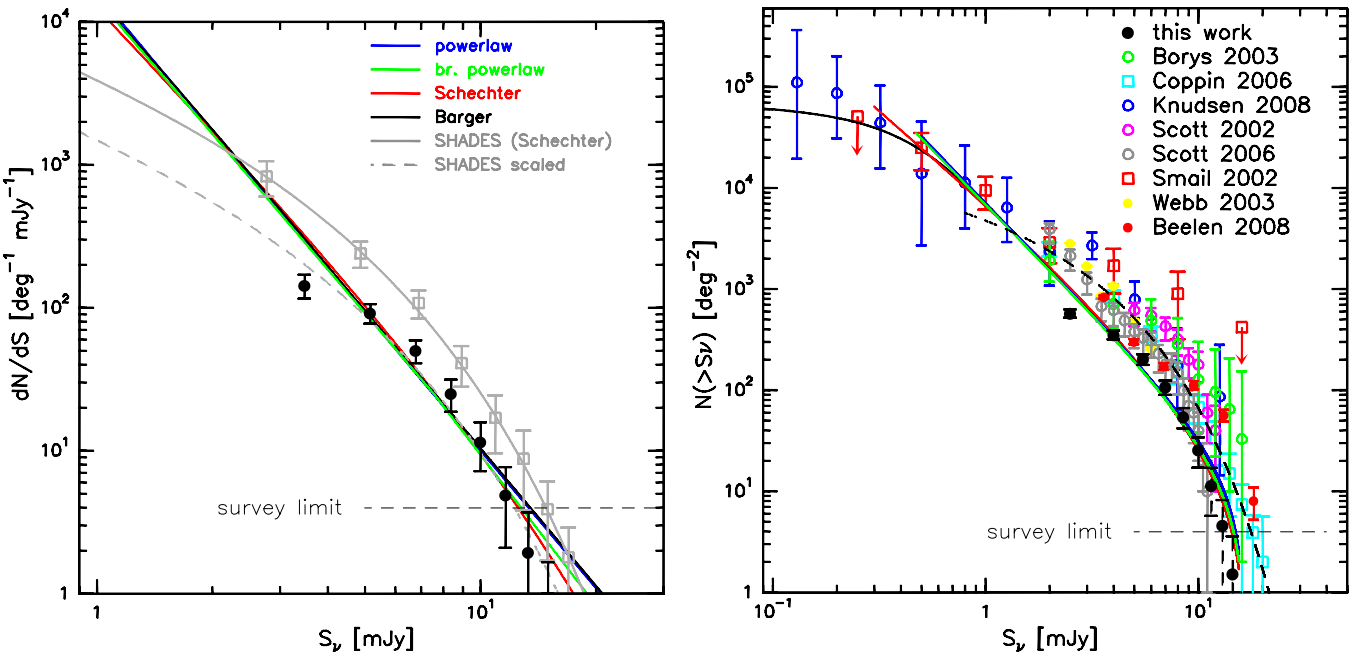

Figure 10. Left: differential source counts for the ECDFS. The colored lines show the results from the $P(D)$ analysis with functional parameters as given in Table 2. The black data points show the results from a Bayesian approach to estimate the source counts from the source catalog. The gray data points are the differential number counts from the SHADES survey (Coppin et al. 2006), the gray line shows their best-fitting Schechter function. The dashed gray line is the SHADES Schechter function with N' scaled to fit our Bayesian source counts. Note that this source count function does not reproduce the observed flux density histogram of the map well (Figure 9). Right: cumulative number counts for the ECDFS compared to other studies. The black data points represent the direct sum of the differential counts shown in the left part of the figure, the solid lines are integrals over the results of the $P(D)$ analysis, the dashed line shows the best-fitting Schechter function from Coppin et al. (2006) for SHADES.

(A color version of this figure is available in the online journal.)

Table 2
Best-fitting Parameters of the Differential Source Counts to the Observed Flux Histogram

Fit	[a]Y	S′ (mJy)	N' (deg^{-2} mJy^{-1})	α	β	$S_{\rm min}$ (mJy)	EBL (Jy deg^{-2})
Power law	$(\frac{S}{S'})^{-\alpha}$	[b]5.0	93	3.2	···	0.5	29.1
br. power law	$(\frac{S}{S'})^{-\alpha}$ for $S > S'$						
	$(\frac{S}{S'})^{-\beta}$ for $S < S'$	7.6	25	3.5	3.1	0.5	29.5
Schechter fct.	$(\frac{S}{S'})^{-\alpha}\, e^{-S/S'}$	10.5	21.5	2.7	···	0.3	33.1
Barger fct.	$\frac{1}{1+(\frac{S}{S'})^{\alpha}}$	0.56	106000	3.2	···	···	32.0

Notes.
[a] Counts are parameterized as $\frac{dN}{dS} = N' \times Y$.
[b] S' fixed to 5.0 mJy.

et al. 2006) which is comparable in size, but has a noise level ∼2 higher than LESS.

For comparison to previous work, we derived the cumulative source counts by directly summing over the differential source counts derived above. The cumulative source counts are shown in comparison to other studies in Figure 10 (right). In this figure, we also show the integrals over the functions fitted by our $P(D)$ analysis (Table 2).

3.4. Two-point Correlation

We have investigated the clustering properties of the SMGs in the ECDFS by means of an angular two-point correlation function. $w(\theta)$ and its uncertainty was computed using the Landy & Szalay (1993) estimator. The random catalog was generated from the same simulations we used for our completeness estimate (Section 3.2.2). To generate random positions of the sources we used the LINUX random number generator (Gutterman et al. 2006). The angular two-point correlation is presented in Figure 11. We detect positive clustering for angular scales below ∼1′, although only the smallest angular scale (20″–50″ bin) shows statistically significant clustering (3.4σ). For comparison to other studies we fit the angular correlation by a single power law using

$$w(\theta) = A_w\,(\theta^{(1-\gamma)} - C), \tag{9}$$

where C accounts for the bias to lower values of the observed compared to the true correlation (see, e.g., Brainerd & Smail 1998). As our data are too noisy to fit all three parameters, we fixed γ to 1.8 which has been used in many other studies (e.g., Daddi et al. 2000; Farrah et al. 2006; Hartley et al. 2008). This yields $A_w = 0.011 \pm 0.0046$ and $C = 12.4 \pm 2.5$ or a characteristic clustering angle of $\theta_0 = 14'' \pm 7''$. We also calculated C directly from our random catalog using Equation (22) from Scott et al. (2006) and assuming $\gamma = 1.8$. This yields $C = 4.5$ and $A_w = 0.007 \pm 0.004$ ($\theta_0 = 7'' \pm 5''$) for a single parameter fit of Equation (9) to our data. These numbers

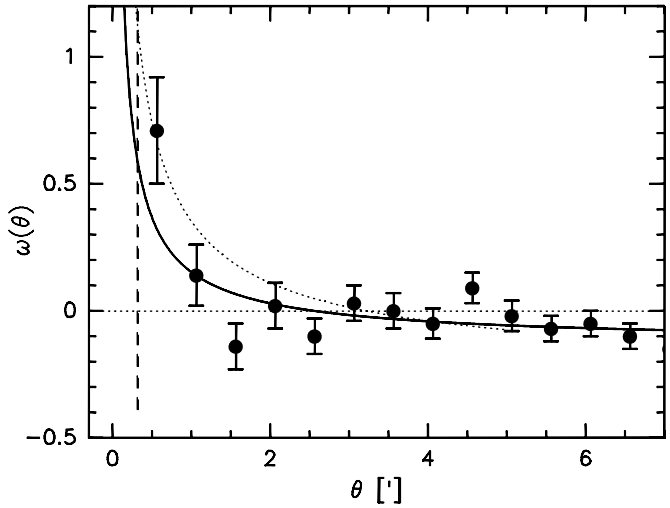

Figure 11. Observed angular two-point correlation function. The solid curve shows a power-law fit to the data, the dotted line is the corresponding function derived for SMGs selected from a variety of surveys by Scott et al. (2006). The dashed vertical line shows the size of the LABOCA beam.

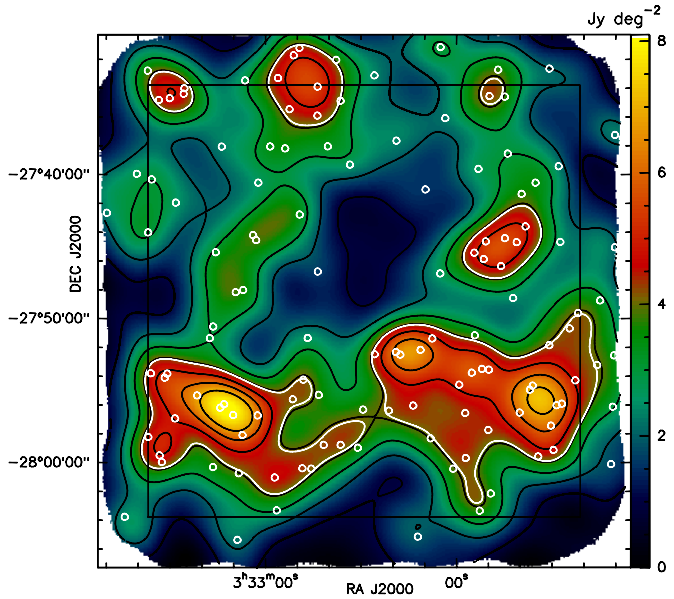

Figure 12. 870 μm flux density distribution smoothed to 5′ spatial resolution. The flux density is shown in Jy deg^{-2}. The black square shows the central 30′ × 30′ of the ECDFS. The white circles mark the location of the 126 sources listed in Table 1. Black contours are shown from 1 to 7 Jy deg^{-2} spaced by 1 Jy deg^{-2}. The white contour is the 4.1 Jy deg^{-2} level that has been used to define the SMG over- and underdensity regions.

(A color version of this figure is available in the online journal.)

demonstrate that the it remains difficult to derive the strength of the SMG clustering from our data but also that higher spatial resolution would greatly help to identify close SMG pairs for a better determination of the clustering.

4. DISCUSSION

4.1. Source Counts

The source counts derived from our $P(D)$ analysis show a reasonable agreement with the direct estimate from the source catalog (Figure 10). We find, however, that the direct counts yield significantly lower number counts for flux densities of ∼3 mJy and somewhat higher counts for ∼7 mJy compared to the $P(D)$ counts. The direct counts therefore suggest a deviation from a single power law with a break between 5 and 7 mJy, similar to the break found by Coppin et al. (2006) for the SHADES survey and by Knudsen et al. (2008) for the Leiden SCUBA Lens Survey. This is shown in Figure 10 (left) where we plot the best-fitting Schechter function for the SHADES survey (Coppin et al. 2006) with N' adjusted to fit our direct counts. This comparison suggests a similar shape (but different normalization) of the source counts between LESS and SHADES. A comparison of the resulting flux density histogram of this model ($P(D)$ like diagram) to the observations, however, clearly shows a significant deviation of the pixel counts for flux densities below ∼4 mJy (Figure 9).

The most likely explanation for this discrepancy is that the direct source count method does not take multiple sources in the beam into account, but assumes that the de-boosted flux density arises from a single source. However, from our Monte Carlo simulations we find that this assumption is poorly justified for LESS. For differential counts following a single power law as given in Table 2, we find that 25% of the extracted sources in the simulations are in fact multiple sources that fall too close together (and/or have too poor signal to noise) to be identified as double sources. As these multiple sources are recovered as a single source in the extraction, this naturally leads to an underestimate of the faintest sources while overestimating counts at higher flux densities. This explains the observed differences between both methods and therefore we are confident that the $P(D)$ analysis (which does take source overlap into account) yields more reliable results on the shape of the submillimeter source counts. We note that for the source counts derived from the SHADES survey, Coppin et al. (2006) used a correction factor determined from Monte Carlo simulations to take the underestimate of the faintest sources into account.

In any case, both methods show consistently that submillimeter number counts in the ECDFS are significantly lower for flux densities above ∼3 mJy compared to any other deep fields observed at 850 μm so far. Using the SHADES number counts for comparison (which are representative also for other fields observed with SCUBA, see Figure 10) we find that the cumulative source counts of the ECDFS are smaller by a factor of ∼2 for flux densities above 3 mJy. This is in line with results from optical/NIR surveys which revealed that several restframe-optical populations are underabundant in the CDFS compared to other deep fields: van Dokkum et al. (2006) showed that massive K-band-selected galaxies at redshift >2 are underabundant by 60%, Marchesini et al. (2007) reported a mild underdensity of $z > 2.5$ DRGs, and Dwelly & Page (2006) reached similar conclusions for optically bright AGNs at high redshifts. These studies only covered the central 15′ × 15′ of the field where the submillimeter source density is even lower than in the full field (see Section 4.3 and Figure 12). Similar underdensities have also been reported in the 30′ × 30′ ECDFS for BzKs (Blanc et al. 2008) as well as for X-ray-selected sources (Lehmer et al. 2005; Luo et al. 2008). The central region of the ECDFS is also underdense in faint ($S_{1.4\,\mathrm{GHz}} \approx 40$ μJy) radio sources (E. Ibar 2009, private communication). We note, however, that the SMG underdensity is only observed for bright sources. Due to the steep slope and the lack of evidence for a flattening of the source counts from our $P(D)$ analysis for low fluxes, our number counts become consistent with results derived for the faint end of the SMG population in gravitationally lensed fields at flux densities of ∼1 mJy (Smail et al. 2002; Knudsen et al. 2008).

4.2. Clustering

Evidence for strong clustering of SMGs first emerged from overdensities of SMGs in close proximity to other high-redshift objects (e.g., Ivison et al. 2000; Chapman et al. 2001; Stevens et al. 2004; Kneib et al. 2004; Beelen et al. 2008). Direct measurements of three- and two-dimensional clustering of SMGs have been presented by Blain et al. (2004), Greve et al. (2004), and Scott et al. (2006). Due to the small number of sources typically involved in these studies, the significance of the clustering amplitude, however, remains marginal. Although the number of sources detected by us in the ECDFS only gives a small improvement in terms of signal to noise compared to the previous measurements, our detection of strong clustering in an independent submillimeter survey greatly improves the reliability of SMG clustering results.

Our characteristic clustering angle of $\theta_0 \approx 5''$–$15''$ is smaller than the angle of $\theta_0 \approx 40''$–$50''$ derived by Scott et al. (2006) but in agreement with the predictions of merger models (van Kampen et al. 2005), which predict clustering scales between $5''$ (for a hydrodynamical model) and $20''$ (for a high mass merger model). The difference between our results and those by Scott et al. (2006) can most likely be explained by the small significance of the clustering signal in both studies. From Figure 11 it can be seen that the power-law fit by Scott et al. (2006) is consistent with our most significant data point at an angular distance of $40''$ and that our smaller clustering angle mainly results from the small angular correlation for distances between $1'$ and $2'$ in our data. However, Greve et al. (2004) also presented evidence for an excess of SMG pairs with a typical separation of $23''$ based on 1.2 mm observations which appears to support our findings. We note that the angular correlation function should not be affected by the LSS filtering of our map because it refers to the angular separation between point sources which remains unaffected by the filtering.

A comparison of the clustering of SMGs to other high-redshift source populations has the potential to shed more light on the evolution of SMGs and to investigate to what kind of sources SMGs evolve once the gas has been consumed. The clustering, however, is expected to evolve with redshift (e.g., Farrah et al. 2006) and a conclusive comparison of the clustering relies on a three-dimensional clustering analysis which requires knowledge of the redshift distribution of our SMGs. Assuming the same redshift distribution for our SMGs as the distribution used by Farrah et al. (2006; a Gaussian centered at $z = 2.5$ with an FWHM of 1.2, similar to the redshift distribution of SMGs derived by Chapman et al. 2005) our data suggests a correlation length of $r_0 = 10 \pm 6\,h^{-1}$ Mpc and $r_0 = 13 \pm 6\,h^{-1}$ Mpc for our single and two parameter fits, respectively. These values are larger than, but consistent within the errors with, the correlation length of $r_0 = 6.9 \pm 2.1\,h^{-1}$ Mpc derived by Blain et al. (2004) for SMGs and in good agreement with the correlation length of $r_0 = 14.4 \pm 2.\,h^{-1}$ Mpc derived for 24 μm selected ULIRGs at $z = 2$–3 (Farrah et al. 2006).

Most models for the evolution of overdensities over time predict an increasing correlation length for decreasing redshift (for a collection of evolution models see, e.g., Overzier et al. 2003). This suggests that the successors of SMGs could be associated with clusters of galaxies ($r_0 \approx 20\,h^{-1}$ Mpc) at the present epoch. Comparing our clustering strength to the correlation length of dark matter (DM) halos as a function of redshift (e.g., Matarrese et al. 1997) furthermore suggests that SMGs reside in more massive ($\sim 10^{13}$–$10^{14}\ M_\odot$) DM halos than other high-z source populations such as Lyman-break galaxies (LBGs) and QSOs. Given the uncertainties of our measurement, the unknown redshift distribution of our SMGs and the model dependence of the DM clustering these numbers are quite uncertain but support the conclusions of previous studies (Blain et al. 2004; Farrah et al. 2006).

4.3. Spatial Variations of the Source Counts

Motivated by the strong clustering detected in the distribution of the submillimeter sources we also investigated the spatial variations of the source counts across the map. To distinguish between regions with potential over and underdensities of submillimeter sources we have used the integrated extragalactic 870 μm flux detected in the map as reference. The variations were calculated at a spatial resolution of $5'$ by convolving the flux map by a Gaussian kernel. The resulting flux distribution is shown in Figure 12 in units of Jy deg^{-2} and reflects mainly the large-scale distribution of the individually detected sources as faint extended emission has been removed by our optimal point-source filtering operation (see Section 2). We have used the 4.1 Jy deg^{-2} contour to divide our source catalog into two sub-catalogs which we call for convenience the "sparse" and the "dense" region in the following. The contour was chosen to give roughly an equal number of detected sources for both catalogs. The source selection based on the large-scale flux distribution emphasizes the difference of the source counts between over and underdensities and is no longer representative for the counts in a blank field survey.

The source counts were determined in the same manner as described in Section 3.3 using a $P(D)$ analysis and a direct estimate of the source counts. In the top panel of Figure 13, we show the observed flux histograms for both regions in comparison to the fits from the $P(D)$ analysis. For the sparse region we find that the source counts are well described by a single power law. The best-fitting model yields a normalization at 5 mJy half of that for the full field ($N' = 47 \pm 8\,\mathrm{deg}^{-2}\,\mathrm{mJy}^{-1}$) and a slope of $\alpha = 3.6 \pm 0.3$—steeper than the counts for the full field ($\alpha = 3.2 \pm 0.2$). The $P(D)$ analysis suggests that the source counts of the dense region are much shallower. For a single power law we find good matching parameters of $N' = 250 \pm 20\,\mathrm{deg}^{-2}\,\mathrm{mJy}^{-1}$ and $\alpha = 2.9 \pm 0.2$. The fitting, however, suggests that the counts are slightly better described by a broken power law or a Schechter function. For a broken power law the break occurs at $\approx$8 mJy with a normalization of $N' = 100 \pm 8\,\mathrm{deg}^{-2}\,\mathrm{mJy}^{-1}$. For the slopes we find $\alpha = 2.4 \pm 0.15$ and $\beta = 4.7 \pm 0.6$. In the bottom part of Figure 13, we compare the integrated source counts determined from the direct source count estimate and the $P(D)$ analysis for both regions to the counts of other 870 μm surveys. Figure 13 shows that the source counts for the dense region are in good agreement with results of the SHADES and other submillimeter surveys. This comparison demonstrates that (1) the surface density of submillimeter sources is not constant, but changes by a factor $\sim$3 on angular scales of $\sim 10'$ and (2) the sampling variance is not due to a simple scaling of the number counts but associated with changes of the shape of the source counts. The latter finding suggests that the sampling variance is not due to (weak) lensing by foreground mass distributions but intrinsic to the distribution of submillimeter sources.

4.4. Contribution to the EBL

The $P(D)$ analysis of the differential source counts also provides an estimate on the integrated 870 μm background light

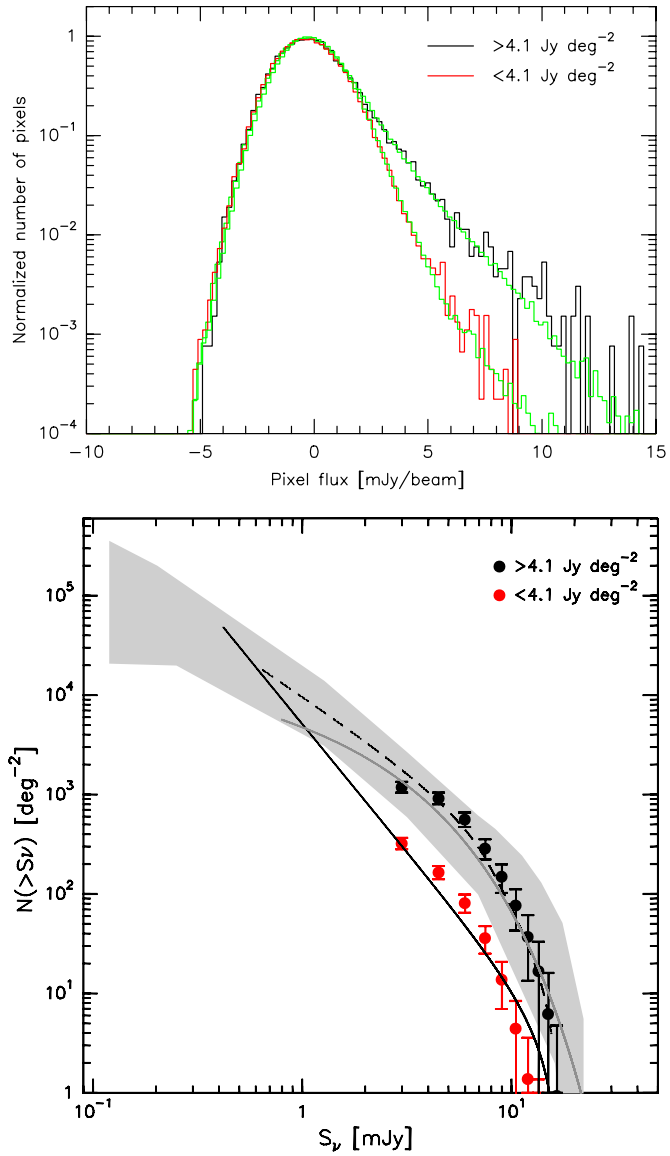

Figure 13. Variation of the source counts with source surface density: top: the black and the red histograms show the pixel flux distribution for the dense and sparse region (Figure 12). The green curves show the results from our $P(D)$ analysis. All histograms are normalized to a peak value of 1. Bottom: integrated source counts in both subregions. The data points are the source counts derived from the direct estimate, the black lines the results from the $P(D)$ analysis. The gray line shows the SHADES source counts, the gray area the source counts derived by other 870 μm studies (see Figure 10, right).

(A color version of this figure is available in the online journal.)

that can be compared to the interpolated EBL at submillimeter wavelength from *COBE FIRAS* of ∼45 Jy deg^{-2} (Puget et al. 1996; Fixsen et al. 1998). Depending on the assumed underlying source distribution we recover an EBL contribution of 29–32 Jy deg^{-2} for the ECDFS (see Table 2). We note that this range is a lower limit to the true underlying 870 μm flux as the contribution of very faint sources, which are expected to form an almost uniform distribution across the field at the spatial resolution of LABOCA, will be removed from our data in the correlated noise removal steps. In comparison to the values measured by *COBE*, we therefore detect >65%–70% of the EBL for sources brighter than ∼0.5 mJy (which corresponds to a typical lower flux cutoff in our $P(D)$ analysis). These numbers demonstrate that it is unlikely that the integrated EBL level in the ECDFS is significantly lower than in other parts of the sky. This implies that the observed factor 2 underdensity of submillimeter source relative to other deep fields is restricted to ULIRGs with far-infrared luminosities of $>2 \times 10^{12}$ $L_{\odot}$ (assuming no lensing and $z > 0.5$ for the bulk of our sources), while more typical star-forming galaxies, which dominate the EBL, are not underabundant in the field. This conclusion is also supported by the intensity of the EBL we find for the two subregions discussed in Section 4.3, where our $P(D)$ analysis does not yield a significant difference between the two fields.

5. SUMMARY AND CONCLUSIONS

We have presented a deep 870 μm survey of the ECDFS using LABOCA on the APEX telescope at Llano de Chajnantor in Chile. This is the largest contiguous deep submillimeter survey to date. Our map has a highly uniform noise level across the full 30′ × 30′ field of 1.2 mJy beam^{-1} and our survey is >95% complete for sources down to a flux limit of 6.5 mJy. Our main findings are summarized as follows.

1. At the (beam smoothed) spatial resolution of 27″ of our survey we find that the map's noise level is affected by confusion noise arising from faint, individually undetected SMGs. From the rms noise as a function of integration time we derive a confusion noise of $\sigma_c \approx 0.9$ mJy beam^{-1}.
2. We identify 126 submillimeter sources in a search area of 1260 arcmin^2 above a signal to noise threshold of 3.7σ, which corresponds to an expected FDR of five sources.
3. We have determined the differential and integrated source counts using a $P(D)$ analysis and an estimate based on our source catalog. Both results are in reasonable agreement and show that SMGs in the ECDFS are underabundant by a factor of ∼2 for sources brighter than 3 mJy compared to the average of previous surveys. Under the assumption that the bulk of the sources is at $z > 0.5$, this implies an underdensity of ULIRGs with $L_{\rm FIR} > 2 \times 10^{12}$ $L_{\odot}$ compared to other blank fields that have been observed in the submillimeter. The source counts are well described by a single power law with a slope of $\alpha = 3.2 \pm 0.2$.
4. We derive the angular two-point correlation function for the SMGs and find clustering on angular scales <1′ with a significance up to 3.4 σ. Assuming a power-law dependence for the correlation function we derive a clustering amplitude of $A_w = 0.011 \pm 0.0046$ or a characteristic angular scale of $\theta_0 = 14'' \pm 7''$ for $\gamma = 1.8$. Assuming a redshift distribution similar to that observed for spectroscopically confirmed SMGs, we derive a correlation length of $r_0 = 13 \pm 6\, h^{-1}$ Mpc, somewhat larger than previous estimates of the three-dimensional clustering of SMGs but in agreement with the clustering derived for 24 μm selected ULIRGs.
5. We have investigated for the first time the spatial variations of the SMG source counts. We find that the differential source counts in regions with an overdensity of SMGs have a different shapes compared to those with underdensities. While the counts in underdense regions are well fitted by a single power law with a slope of $\alpha = 3.6 \pm 0.3$, the counts in the overdensities are significantly shallower with $\alpha = 2.9 \pm 0.2$. The counts in the overdensities are slightly better described by a broken power law or a Schechter function. For flux densities below 8 mJy we find a slope of $\alpha = 2.4 \pm 0.15$, for sources above this limit the counts are much steeper with $\beta = 4.7 \pm 0.6$. This may indicate

an intrinsic turnover in the underlying luminosity function placing an upper limit on the FIR luminosity.

6. The integrated 870 μm flux density derived from our survey is >29–32 Jy deg^{-2} for sources brighter than $\sim$0.5 mJy which corresponds to $>65\%$–70% of the EBL estimated from *COBE* measurements. We do not find a significant difference of the quantity between SMG over- and underdensities. We conclude that ECDFS is underabundant of ULIRGs but not of more typical star-forming systems with lower FIR luminosities, which dominate the EBL.

We thank the APEX staff for their aid in carrying out the observations. APEX is operated by the Max-Planck-Institut für Radioastronomie, the European Southern Observatory, and the Onsala Space Observatory. I.R.S., K.E.K.C., and R.J.I. acknowledge support from STFC. J.S.D. acknowledges the support of the Royal Society and of STFC.

REFERENCES

Austermann, J. E., et al. 2009, MNRAS, 393, 1573
Barger, A. J., Cowie, L. L., & Sanders, D. B. 1999, ApJ, 518, 5
Beckwith, S. V. W., et al. 2006, AJ, 132, 1729
Beelen, A., et al. 2008, A&A, 485, 645
Bertoldi, F., et al. 2007, ApJS, 172, 132
Blain, A. W., Chapman, S. C., Smail, I., & Ivison, R. 2004, ApJ, 611, 725
Blain, A. W., Smail, I., Ivison, R. J., & Kneib, J. P. 1999, MNRAS, 302, 632
Blanc, G., A., et al. 2008, ApJ, 681, 1099
Borys, C., Chapman, S. C., Halpern, M., & Scott, D. 2003, MNRAS, 334, 385
Brainerd, T., G., & Smail, I. 1998, ApJ, 494, 137
Caldwell, J. A. R., et al. 2008, ApJS, 174, 136
Chapman, S. C., Blain, A. W., Smail, I., & Ivison, R. J. 2005, ApJ, 622, 772
Chapman, S. C., Lewis, G. F., Scott, D., Richards, E., Borys, C., Steidel, C. C., Adelberger, K. L., & Shapley, A. E. 2001, ApJ, 548, 17
Condon, J. J. 1974, ApJ, 188, 279
Coppin, K., Halper, M., Scott, D., Borys, C., & Chapman, S. 2005, MNRAS, 357, 1022
Coppin, K., et al. 2006, MNRAS, 372, 1621
Coppin, K., et al. 2009, MNRAS, 395, 1905
Cowie, L. L., Barger, A. J., & Kneib, J. P. 2002, AJ, 123, 2197
Daddi, E., Cimatti, A., Pozzetti, L., Hoekstra, H., Röttgering, H. J. A., Renzini, A., Zamorani, G., & Mannucci, F. 2000, A&A, 361, 535
Damen, M., Labbe, I., Franx, M., van Dokkum, P. G., Taylor, E. N., & Gawiser, E. J. 2009, ApJ, 690, 937
Devlin, M. J., et al. 2009, Nature, 458, 737
Dwelly, T., & Page, M. J. 2006, MNRAS, 372, 1755
Farrah, D., et al. 2006, ApJ, 641, 17
Fixsen, D. J., Dwek, E., Mather, J. C., Bennett, C. L., & Shafer, R. A. 1998, ApJ, 508, 123
Gawiser, E., et al. 2006, ApJS, 162, 1
Giacconi, R., et al. 2002, ApJS, 139, 369
Giavalisco, M., et al. 2004, ApJ, 600, 93
Güsten, R., Nyman, L. A., Schilke, P., Menten, K. M., Cesarsky, C., & Booth, R. 2006, A&A, 454, 13
Gutterman, Z., Pinkas, B., & Reinman, T. 2003, Proc. IEEE Symp. Secur. Priv., 38, 371
Greve, T. R., Pope, A., Scott, D., Ivison, R. J., Borys, C., Conselice, C. J., & Bertoldi, F. 2008, MNRAS, 389, 1489
Greve, T. R., et al. 2004, MNRAS, 354, 779
Greve, T. R., et al. 2009, ApJ, submitted (arXiv:0904.0028)
Hartley, W. G., et al. 2008, MNRAS, 391, 1301
Hogg, D. W., & Turner, E. L. 1998, PASP, 110, 727
Hopkins, A. M., Miller, C. J., Connolly, A. J., Genovese, C., Nichol, R. C., & Wasserman, L. 2002, AJ, 123, 1086
Hughes, D., et al. 1998, Nature, 394, 241
Isaak, K. G., et al. 2002, MNRAS, 329, 149
Ivison, R. J., Dunlop, J. S., Smail, I., Dey, A., Liu, M. C., & Graham, J. R. 2000, ApJ, 542, 27
Ivison, R. J., Smail, I., Le Borgne, J.-F., Blain, A. W., Kneib, J.-P., Bezecourt, J., Kerr, T. H., & Davies, J. K. 1998, MNRAS, 298, 583
Ivison, R. J., et al. 2007, MNRAS, 380, 199
Ivison, R. J., et al. 2009, MNRAS, in press (arXiv:0910.1091)
Kneib, J., van der Werf, P. P., Kraiberg Knudsen, K., Smail, I., Blain, A., Frayer, D., Barnard, V., & Ivison, R. 2004, MNRAS, 349, 1211
Knudsen, K. K., van der Werf, P. P., & Kneib, J. P. 2008, MNRAS, 384, 1611
Kovács, A. 2008, Proc. SPIE, 7020, 45
Kovács, A., Chapman, S. C., Dowell, C. D., Blain, A. W., Ivison, R. J., Smail, I., & Phillips, T. G. 2006, ApJ, 650, 592
Landy, S. D., & Szalay, A. S. 1993, ApJ, 412, 64
Laurent, G. T., et al. 2005, ApJ, 623, 742
Le Floch, E., et al. 2005, ApJ, 632, 169
Lehmer, B. D., et al. 2005, ApJS, 161, 21
Luo, B., et al. 2008, ApJS, 179, 19
Maloney, P. R., et al. 2005, ApJ, 635, 1044
Marchesini, D., et al. 2007, ApJ, 656, 42
Matarrese, S., Coles, P., Lucchin, F., & Moscardini, L 1997, MNRAS, 286, 115
Miller, N. A., Fomalont, E. B., Kellermann, K. I., Mainieri, V., Norman, C., Padovani, P., Rosati, P., & Tozzi, P. 2008, ApJS, 179, 114
Overzier, R. A., Röttgering, H. J. A., Rengelink, R. B., & Wilman, R. J. 2003, A&A, 405, 53
Peacock, J. A., et al. 2000, MNRAS, 318, 535
Perera, T. A., et al. 2008, MNRAS, 391, 1227
Pope, A., et al. 2006, MNRAS, 370, 1185
Press, W. H., Flannery, B. P., & Teukolsky, S. A. 1986, Numerical Recipes: The Art of Scientific Computing (Cambridge: Cambridge Univ. Press)
Puget, J. L., Abergel, A., Bernard, J. P., Boulanger, F., Burton, W. B., Desert, F. X., & Hartmann, D. 1996, A&A, 308, 5
Sanders, D. B., & Mirabel, I. F. 1996, ARA&A, 34, 749
Scott, S. E., Dunlop, J. S., & Serjeant, S. 2006, MNRAS, 370, 1057
Scott, S. E., et al. 2002, MNRAS, 331, 817
Scott, K. S., et al. 2008, MNRAS, 385, 2225
Serjeant, S., et al. 2003, MNRAS, 344, 887
Siringo, G., et al. 2009, A&A, 497, 945
Smail, I., Ivison, R. J., & Blain, A. W. 1997, ApJ, 490, 5
Smail, I., Ivison, R. J., Blain, A. W., & Kneib, J. P. 2002, MNRAS, 331, 495
Stevens, J. A., Page, M. J., Ivison, R. J., Smail, I., & Carrera, F. J. 2004, ApJ, 604, 17
Taylor, E. N., et al. 2009, ApJS, 183, 295
van Dokkum, P. G., et al. 2006, ApJ, 638, 59
van Kampen, E., et al. 2005, MNRAS, 359, 469
Webb, T. M., et al. 2003, ApJ, 587, 41
Wolf, C., et al. 2004, A&A, 421, 913
Wolf, C., Hildebrandt, H., Taylor, E. N., & Meisenheimer, K. 2008, A&A, 492, 933
Younger, J. D., et al. 2008, ApJ, 688, 59